7-2022

Light Curves from Convective Common Envelopes in Low-Mass Binaries

Nikki G. Noughani
ngn8219@rit.edu

Light Curves from Convective Common Envelopes in Low-Mass Binaries

By

Nikki G. Noughani

A thesis submitted in partial fulfillment of the requirements for the degree of M.S. in Astrophysical Sciences and Technology, in the College of Science, Rochester Institute of Technology.

July, 2022

Approved by

Dr. Andrew Robinson	Date
Director, Astrophysical Sciences and Technology	

Approval Committee: Jason Nordhaus, Joshua Faber, Joel Kastner

ASTROPHYSICAL SCIENCES AND TECHNOLOGY
COLLEGE OF SCIENCE
ROCHESTER INSTITUTE OF TECHNOLOGY
ROCHESTER, NEW YORK

CERTIFICATE OF APPROVAL

M.S. DEGREE THESIS

The M.S. Degree Thesis of *Nikki G. Noughani* has been examined and approved by the thesis committee as satisfactory for the thesis requirement for the M.S. degree in Astrophysical Sciences and Technology.

Dr. Joshua Faber, Committee Member

Dr. Joel Kastner, Committee Member

Dr. Jason Nordhaus, Thesis Advisor

Date

Acknowledgements

I would like to thank Dr. Jason Nordhaus for advising me through this project, as well as Dr. Emily C. Wilson for all her help with understanding her work and its implementation in this work. I'd like to thank everyone in the AST department who taught me all I needed to know and more. I'd also like to thank Dr. Ralf Kotulla, who first introduced me to research involving light curves. And I'd like to thank my family for all their support. I would finally like to thank Dr. Jason Nordhaus, Dr. Joel Kastner, and Dr. Josh Faber for serving on my Master's committee.

Abstract

The presence of an orbiting companion can significantly affect the evolution of a star. For close binaries, radial expansion of the primary's envelope during the post-Main Sequence, coupled with mass-loss from winds, can destabilize the orbit such that the companion plunges into the primary star. Such common envelope (CE) events are thought to be the primary mechanism for forming close binaries in the universe, as the orbital separation rapidly shrinks. Despite its importance and predicted ubiquity, the details of stellar evolution through the CE phase remain highly uncertain. Here, we construct theoretical light curves for convective CE events. The effects of convection impart a distinct, long-term signature in the light curves, which should be detectable with upcoming transient surveys.

Contents

1 Stellar Evolution

Recorded astronomy began before formal telescopes and tools, using one's eyes to measure the change in sources of light in the sky. While some of these sources were planets reflecting light from the sun, most were stars. The distance to these sources were first determined using parallax, which measures the position of an object in the sky from two different points on Earth or in Earth's orbit. This can be done using any visible source, planet or star. Later it was discovered that a certain family of variable stars change their brightness with relation to their distance. The measured, periodic changes in Cepheid variable stars thus became an important means of calculating distances, even allowing for measurements further than parallax. And to measure distances beyond those of the visible Cepheid stars, astronomers can use Type Ia supernovae explosions (Fernie (1969)). But beyond measuring distance, stars make up the majority of visible light sources, aid in exoplanet discovery, and, as they grow old and die, can leave behind compact remnants. These remnants include white dwarfs, neutron stars, and black holes, which are dense enough to create gravitational waves as they move through space. Stars are also singularly responsible for creating the fundamental elements for life. Therefore, learning how stars evolve over time is the first step in understanding the universe as a whole.

1.1 The Hertzsprung-Russell Diagram

Created independently by two astronomers in the early 1910s, the Hertzsprung-Russell (HR) diagram is a classification of stars according to temperature and luminosity, and reveals clear trends that stars follow throughout their life cycles. These overall patterns in stellar evolution allow for grouping stars based on their evolutionary state and mass. An example of an HR diagram can be seen in Figure 1.

It is important to note that, although the y-axis luminosities are from dim to bright, the x-axis temperature reads from hottest to coolest values. This is because the original diagrams plotted according to distinctive spectral features (classified under the letters O, B, A, F, G, K, and M according to strengths of absorption lines of hydrogen, helium, and metals) on the x-axis. At the time, the sequence was not clear, and, when they were finally known, they were

discovered to correlate with decreasing temperature (O type stars happen to be the hottest, while M type are coolest).

There are two stellar classifications with respect to mass: Low-mass stars, defined as stars with mass less than or equal to 8 $M_\odot$, and high-mass stars, defined as stars with mass greater than 8 $M_\odot$. A note here that some definitions include an intermediate-mass star, where low-mass stars are between 0.1 and 1 $M_\odot$, and intermediate-stars are between 1 and 8 $M_\odot$, but for this work we will define these groups under the single umbrella of low-mass stars. Stars with cores that burn (undergo nuclear fusion) hydrogen to helium are on the longer diagonal branch identified as the Main-Sequence (MS). This branch starts from cooler, dimmer stars (like AB Doradus C in Figure 1) and moves upward toward hotter, brighter stars. There are two general divergences from the MS on the diagram, marked by Giants (also known as the Red Giant Branch (RGB)) and Supergiants. Stars leave the MS for one of these groups once they have finished burning all the hydrogen in their cores and begin burning helium and other heavier elements instead. These stars are characterized by low surface temperatures and high luminosities, as well as large radii. The last grouping shown on the diagram is the White Dwarfs (WD), which represent the final stage of low-mass stars that have blown off their envelopes and left behind a degenerate core.

1.1.1 Proto- and Pre-Main-Sequence Stars

Stars are formed from dense molecular clouds undergoing gravitational collapse onto central cores (Hoyle & Lyttleton (1939)). These cores are known as protostars, which accrete mass from the surrounding cloud in the form of an accretion disk formed by the conservation of angular momentum. Once collapse begins, the force from gravity increases more than the pressure gradient so that, as time passes, the collapse is driven more and more solely by gravity. This phase for a low-mass star like the Sun can last around 500,000 years, and it is here that the parameters for initial stellar masses and planet formation are set (Dunham *et al.* (2014)).

Accretion on a low-mass protostar from the infalling envelop stops when the envelope is

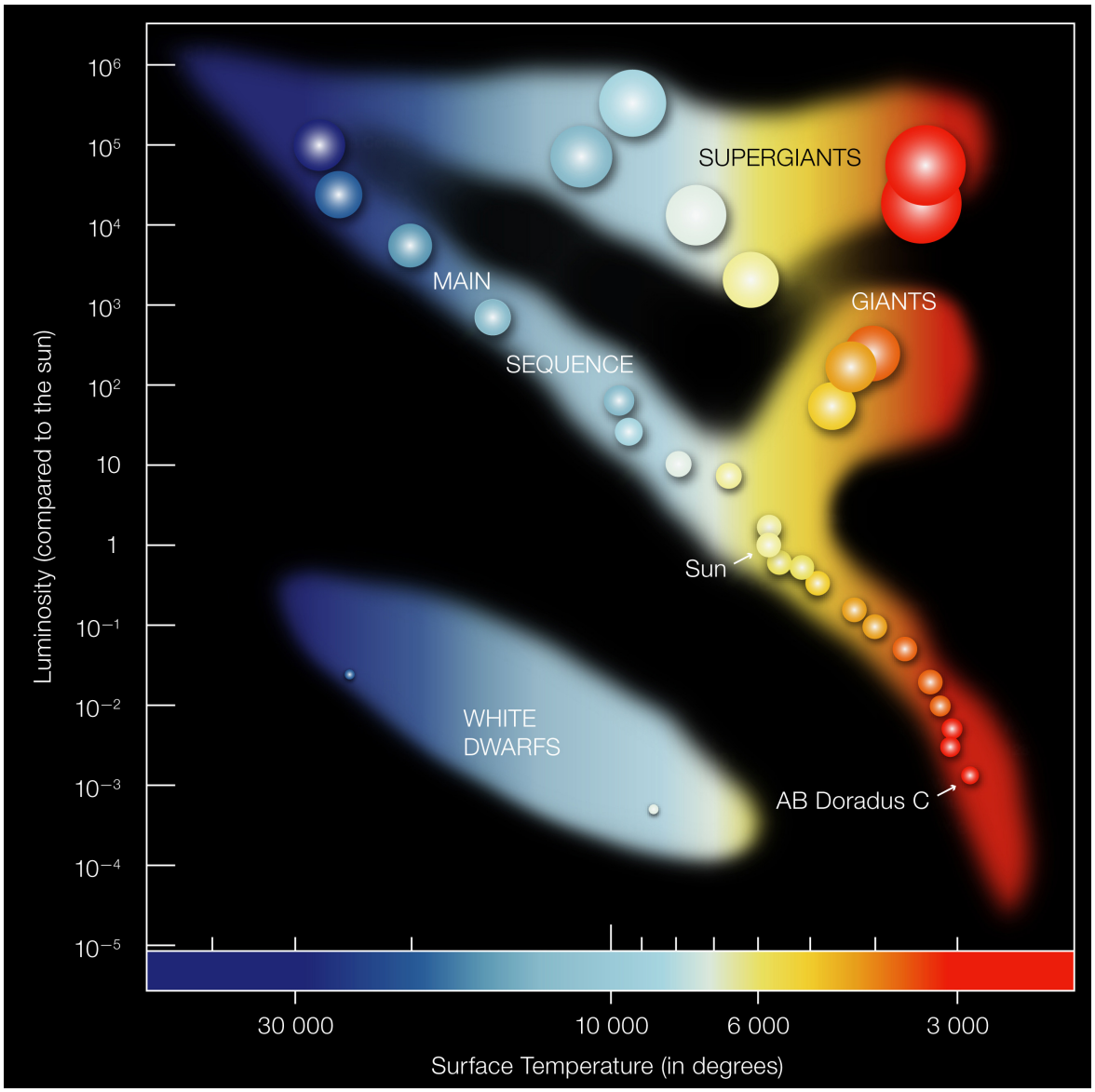

Figure 1: The Hertzsprung-Russell (HR) diagram, taken from ESO (2007), plots the surface temperature of stars against their luminosities. Note that the temperature values are from high to low. There are four main groupings shown: Main-Sequence, Giants, Supergiants, and White Dwarfs. Besides the groupings, two stars are identified in this diagram: the Sun and AB Doradus C. The Sun is a typical Main-Sequence (MS) star that will someday leave the MS and move onto the Red Giant Branch (RGB), identified here with the label Giants. AB Doradus C is one of the lowest mass stars ever found and is a Pre-Main-Sequence (PMS) star. This means AB Doradus C is much cooler and less luminous than the Sun (its luminosity is only about 0.2% that of the Sun's).

blown away, and this occurs before the central temperature required for hydrogen ignition is reached, despite the star having amassed nearly all its final mass. At this stage, the protostar now becomes a pre-Main-Sequence (PMS) star (Larson (2003)). The PMS star will contract, causing its internal temperature to rise. For high mass stars, the accretion will continue well after the core has begun hydrogen burning, meaning these stars will skip the PMS stage entirely before settling on the MS (Hosokawa & Omukai (2009)).

There are a few differences between a protostar and what is considered a fully-realized star. First, the source of light in the protostar phase is produced by gravitational contraction, which causes the gas to be heated and radiate light instead of nuclear fusion. Another way to understand this is that the accreting core of a protostar releases its accretion energy in a thin surface layer, whereas a star's energy source is found in the deep interior. Second, once a hydrostatic core has formed in a protostar there is still significant surface pressure from the infalling gas and dust, whereas stars have surface pressure that is virtually zero. However, the diameter of the accreting core of a protostar in hydrostatic equilibrium is already nearly the size of a star's, so, although it is not undergoing fusion, it is already about as large as the core of the completed star will be (Kippenhahn *et al.* (2012)).

1.1.2 Main-Sequence (MS) Stars

A star moves from the pre-Main Sequence to the Zero Age Main-Sequence (ZAMS) when the contraction in the PMS phase, which causes the core's density, pressure, and temperature to increase, finally heats the core to the limit required for hydrogen burning. Low-mass, ZAMS stars tend to be grouped on a trend line similar to the MS, but slightly higher in luminosity (Palla (2012)). Again, high-mass stars skip this stage altogether and enter on the MS, but the lower the mass of the star, the further away it begins from its eventual entrance point on the MS. Most importantly, as will be discussed in Section 3, the ZAMS marks a more stable phase of evolution for stars. As these stars continue to burn through their hydrogen, they eventually move onto the MS.

Main-Sequence (MS) stars are characterized by nuclear fusion of hydrogen into helium in

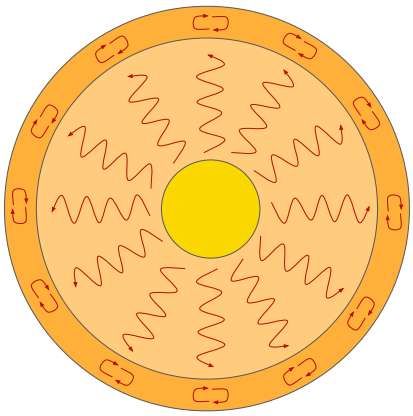

Figure 2: This is a cartoon of the Sun, a typical Main-Sequence (MS) star. The core, in yellow, is where nuclear fusion takes place and has a radius of approximately 1.7×10^{10} centimeters (cm). Next, marked by light orange with arrows moving away from the core is the radiative zone (about 4.2×10^{10} cm wide). After this is the convective zone, marked with circular arrows (about 1.055×10^{10} cm wide). The outermost layers include the photosphere (about 4.5×10^{7} cm wide), chromosphere (about 2.5×10^{8} cm wide), and the corona (not present in every MS star).

their cores (Iben (1967)). Figure 2 shows the interior of the Sun, an example of an MS star. The core, in yellow, has a radius of approximately 1.7×10^{10} centimeters (cm). Exterior to this and marked by a lighter orange color with arrows moving away from the core is the radiative zone. This zone is about 4.2×10^{10} cm wide and is where the thermal energy produced in the core is radiated away towards the surface. After this is the convective zone, marked with circular arrows, which is approximately 1.055×10^{10} cm wide. Here, convection transports energy out towards the surface via the bulk motion of gas parcels, which then cools and circulates back towards the interior where it is reheated and rises again, thus the circular arrows. These three zones mark the interior of the star and are approximately 99.58% of the Sun's volume. The outermost layers include the photosphere (about 4.5×10^{7} cm wide), chromosphere (about 2.5×10^{8} cm wide), and the corona (not present in every MS star). The regions of the star that transport energy from the star's core to the atmosphere are called the stellar envelope.

1.1.3 Red Giant Branch (RGB) Stars

Once a star's core has depleted its supply of hydrogen, the now helium core contracts, during which gravitational potential energy is converted into thermal energy. The internal

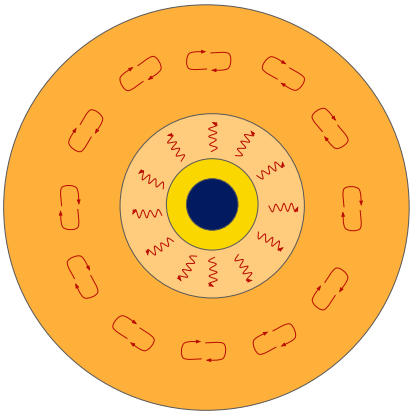

Figure 3: Here is a cartoon of a typical Red Giant Branch (RGB) star. Like an MS star, it includes a convective zone, marked by darker orange and circular red arrows, a radiative zone, marked by light orange with arrows moving away from the core, and even a hydrogen burning zone, marked in yellow. However, the helium core, marked in dark blue, is different, as are the sizes of the zones (here the convective zone is wider than the radiative, whereas an MS star has a wider radiative zone). Also, a RGB star at its largest radius would be hundreds of times larger than its MS counterpart.

layers of the star begin to heat, and eventually the shell of hydrogen surrounding the helium core becomes hot enough to re-start hydrogen fusion. This is where the low-mass stars leave the MS and enter the Red Giant Branch (RGB), marked by Giants in Figure 1. The hydrogen burning shell will generate more energy than the hydrogen burning core did, causing the radiation pressure to increase. Energy is transported to the outer layers of the star via convection (Figure 3). This will cause the star's luminosity to increase drastically, by a factor of 1000 or more, as its radius grows to hundreds of times larger than its MS size.

The evolution between these stages is illustrated in Figure 4. The diagram itself is shown on a simplified HR diagram, which includes temperature and luminosity (note the temperature again is from hot to cool and the luminosity from dim to bright). The diagram shows the steps a Sun-like star would take along the RGB phase, starting from the Solar-type star with a red, hydrogen burning core. Next, as a Red Giant star it has exhausted all the hydrogen in its core, leaving behind a helium core, shown in dark blue, and has begun burning hydrogen in the shell around the core, shown again in red. At its largest radius, the star has heated its envelope as much as it can, preempting a helium flash, which is the sudden onset of helium core fusion. It is important to note that the illustration, particularly at this stage, is not to

scale. This star at the largest radius should be hundreds of times larger than the Solar-type star, which would take up more space than the entire figure has to offer. After this point it becomes a Red clump star. This star is also marked by a red core, but the core is burning helium instead of hydrogen. From here the star can move onto the Horizontal branch and, if it is massive enough, even the Asymptotic Giant Branch, as explained below.

1.1.4 Horizontal Branch and Asymptotic Giant Branch (AGB) Stars

The energy released by the helium flash in the core has several effects, but the most important is a rise in effective temperature and a decrease in surface area, such that the luminosity remains roughly the same. This star will now move left along the horizontal branch of the HR diagram. Horizontal branch stars are characterized by helium core-burning and hydrogen shell-burning. This phase typically lasts on the order of 100 million years for a $1M_{\odot}$ star (Kippenhahn *et al.* (2012)).

Once the helium in the core has been entirely fused into carbon and oxygen, the core will contract again. For a low-mass star, this contraction will not produce enough heat in the core to start another fusion process. However, the now helium shell surrounding the core can begin helium burning as the temperature increases, as can a thin shell of hydrogen above the helium shell. This marks another expansion in radius as the star enters the Asymptotic Giant Branch (AGB) phase (Herwig (2005)).

Once this helium runs low, the outward radiation pressure will start to decrease, meaning the shell of hydrogen gas surrounding the core and layers of heavier elements will contract, heat up, and convert into helium that falls into the helium shell. This produces a thermal pulse that will push out the hydrogen shell until it cools and any hydrogen shell burning ceases.

For a Sun-like star, these pulses can increase the luminosity over tens of thousands of years (Kastner & Wilson (2021)). As these thermal pulses continue from the repeated contraction and expansion of the star, and strong stellar winds develop, the outer layers of the AGB star will be almost entirely ejected, leaving behind an exposed, degenerate core.

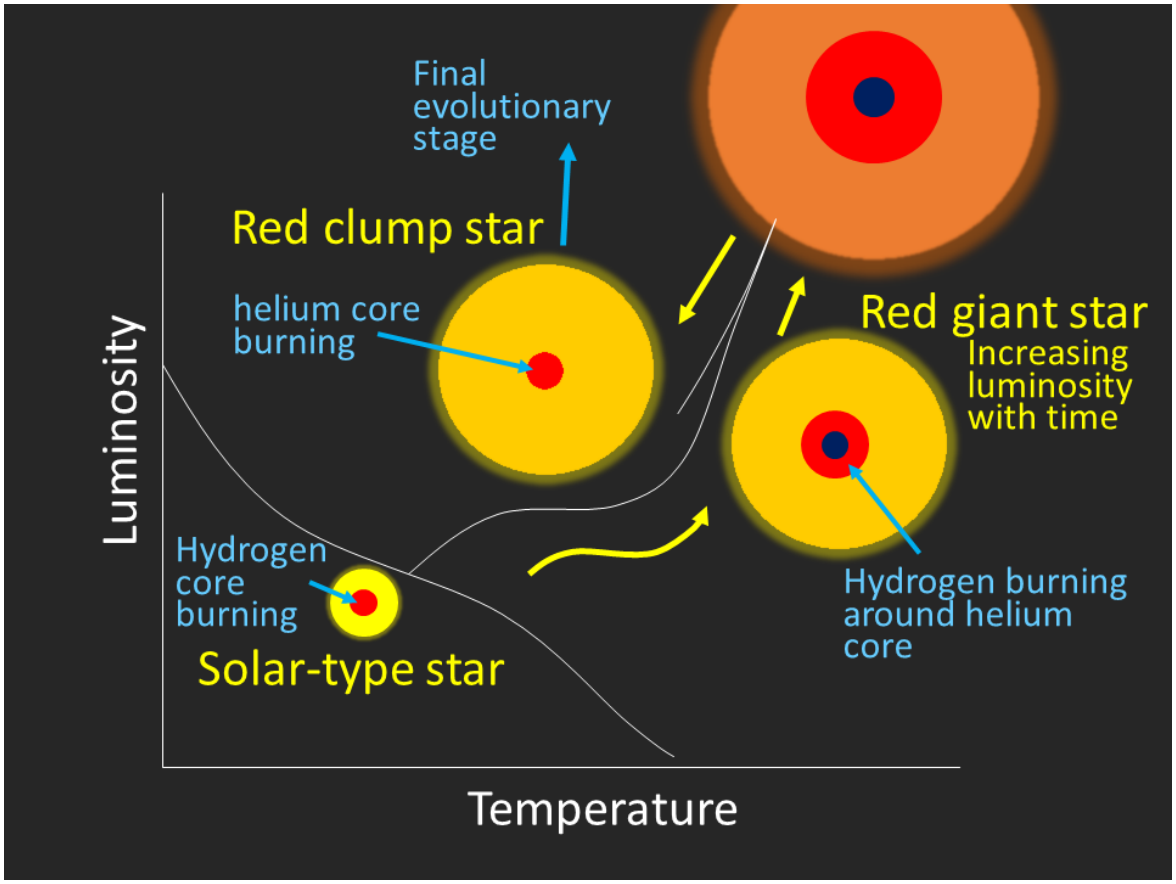

Figure 4: Here the evolution of a Main-Sequence (MS) star through the Red Giant and Asymptotic Giant phase is depicted along a simplified HR diagram (Yan *et al.* (2020)). The temperature is from high to low, and the luminosity from dim to bright. The figures are not to scale. For example, if this were the evolution of our Sun, in its largest radius it would be 256 times its current size, the first position in this diagram. The Red clump star depicted here preempts a phase known as the Asymptotic Giant Branch (AGB), which is explained in more detail in Section 1.1.4. Hydrogen burning in the Solar-type star, as well as the Red giant stars, is shown via the red core and red shells respectively. However, in the Red clump or AGB star the red core represents helium burning instead. The blue core in the two Red giant stars represents a helium core.

1.1.5 White Dwarfs (WDs)

These cores are very hot, with initial temperatures up to 100,000 Kelvin (K), but far less luminous than the RGB or AGB stars, with luminosities of about 1000 times that of our Sun. These temperatures and luminosities will fade significantly over time, with the oldest known cores having temperatures closer to 10,000 K and very low luminosities. And at this point the star has become a White Dwarf (WD) (Figure 1).

WDs are degenerate, meaning that they are extremely dense and "held up" by electron degeneracy pressure as opposed to the radiation and gas pressure of the previous stage of its stellar lifetime. Also, whereas a MS star has a larger radius the more mass it has, a WD has an inverse relationship between mass and size. This means that a WD greater in mass would be smaller in radius than a less massive WD. This is because more massive stellar cores experience a stronger gravitational force and compress more. The heat in a white dwarf is gradually radiated away, but because it has such a small radius, and therefore small surface area, the heat escapes very slowly. It will take a WD tens to hundreds of billions of years to radiate its heat (Liebert (1980)).

1.1.6 Supernovae (SN)

A supernova (SN) is a stellar explosion that releases high amounts of energy and luminosity, about as bright as an entire galaxy of billions of Sun-like stars. A low-mass star will not undergo a SN on its own. However, there are several ways a system can reach the energy limit required for one. These methods of SN are classified by two groups: Type I and Type II.

A Type I SN is, in most cases, a WD in a binary system that is accreting gas from its companion. When the white dwarf has managed to collect enough of this accreted gas (known as the Chandrasekhar limit, this is thought to be when the WD mass goes above 1.4 $M_\odot$ (Mazzali *et al.* (2007))), it produces a thermonuclear explosion that destroys the WD and its companion. These are the brightest kinds of SN and, as mentioned before, can be used to measure the furthest distances in our universe.

A Type II SN occurs in high-mass stars that are at least 8 $M_\odot$ and in the final stage of

their evolution. As the star reaches the point where it can no longer continue nuclear fusion in its core due to a buildup of iron, the outward pressure from this process is eventually overtaken by the inward gravitational force. This results in the star's core collapsing inward to form a neutron star or black hole (BH) as the star's outer layers are pushed outward with incredible force (Weiler & Sramek (1988)).

A note regarding RGB stars and their evolutionary phases. In Section 1.1.3, the process of thermal pulses was described once the star had undergone a helium flash. These pulses produce spikes in luminosity that can be seen in their light curves. However, these pulses are on much longer timescales than a common envelope-induced SN event. Therefore, the likelihood of the two occurring simultaneously is very low. For this reason, these pulses are not included in the light curve models of this work.

1.2 Binary Stars

The review of a single star's evolution above is a highly idealized version of the process, as stars rarely form from a single, isolated cloud of gas. Most often, stars form in clusters in galaxies, meaning there are many additional forces than the ones mentioned. Principal among the effects of stellar evolution in clusters is that stars will develop in multi-body systems where they are gravitationally bound to other nearby objects. A binary star is a system of two stars specifically that are gravitationally bound and therefore orbit one another. At one point in the mid to late twentieth century, it was estimated that 70-80% of MS F and G stars were in binary or multi-star systems. Recently, the number of total binary stars in the universe is estimated to be up to 50%, as the resolution of newer instruments allow for better understandings of bright sources and whether they come from multi-body systems or single stars (Duchêne & Kraus (2013)).

Binaries can be divided into two main groups: wide and close. A wide binary defines a pair of stars that orbit each other at large separations so that they evolve independently. A close binary is a pair of stars that are close enough to transfer matter (usually at 10 astronomical units (AU) (1.496×10^{14} cm) or closer) and therefore evolve together. This mass transfer can,

in some cases, drastically alter the evolutionary paths either of these stars would have taken if in a single system. Close binaries can also be close enough to gravitationally distort one another's outer atmospheres.

1.2.1 Classification of Binaries

While stellar binaries define two stars that are gravitationally bound, there are many different kinds of binaries. Because most stars develop in clusters, they can often become bound to whatever else is forming near them, and, while this does include stars, this also includes planets, neutron stars, BHs and WDs.

There are two classifications used in this project for companions that can produce close binaries after common envelope (CE) events: degenerate and non-degenerate. A degenerate companion, like the WDs from Section 1.1.5, refers to a dense stellar object with extreme gravitational pressure. A non-degenerate companion refers to stars and planets whose internal structures are determined by gas or radiation pressure.

2 Common Envelopes

2.1 Relevance in Astrophysics

In last decade, there has been significant interest in the physics of close binary systems. Driving much of this interest is the Laser Interferometer Gravitational-Wave Observatory (LIGO), which announced the direct detection of its first Gravitational Waves (GWs) in 2016 (Abbott *et al.* (2016)). Those GWs were produced by a BH-BH merger, and, to date, all detected GWs by LIGO have been the products of mergers (Abbott *et al.* (2021); Abbott *et al.* (2020); etc.), meaning they were first in close binaries. Currently, the primary mechanism thought to be responsible for producing close binary end products, pre-merger, is common envelopes (CEs) (Toonen & Nelemans (2013); Kruckow *et al.* (2018); Canals *et al.* (2018)), although they are not the only method being researched (Fabrycky & Tremaine (2007); Thompson (2011); Shappee & Thompson (2013); Michaely & Perets (2016)).

The common envelope (CE) phenomenon was first proposed in Paczynski (1976), and describes the process of an orbiting companion entering the outer layers of a primary star's envelope. The companion can then orbit the primary's core within this now shared envelope. This phase is predicted to last briefly, on the order of a few decades.

2.1.1 The Physics of Common Envelope (CE) Evolution

CE events tend to occur when the primary star in a binary system evolves off the Main-Sequence (MS). The radius of the primary during post-Main-Sequence evolution expands to hundreds of times its original size, significantly increasing the interaction cross section (Ivanova *et al.* (2012); Kochanek *et al.* (2014)). In two-body systems there are several physical effects that can lead to CEs: (i.) direct engulfment, where the radius of the primary far surpasses the orbital separation, (ii.) Roche Lobe overflow, or (iii.) orbital decay via tidal dissipation (Nordhaus & Blackman (2006); Nordhaus *et al.* (2010); Chen *et al.* (2017)). As the binary separation decreases, energy is transferred from the orbit to the CE. If enough energy is released, the envelope becomes unbound and is ejected from the system, leaving a close, post-CE binary.

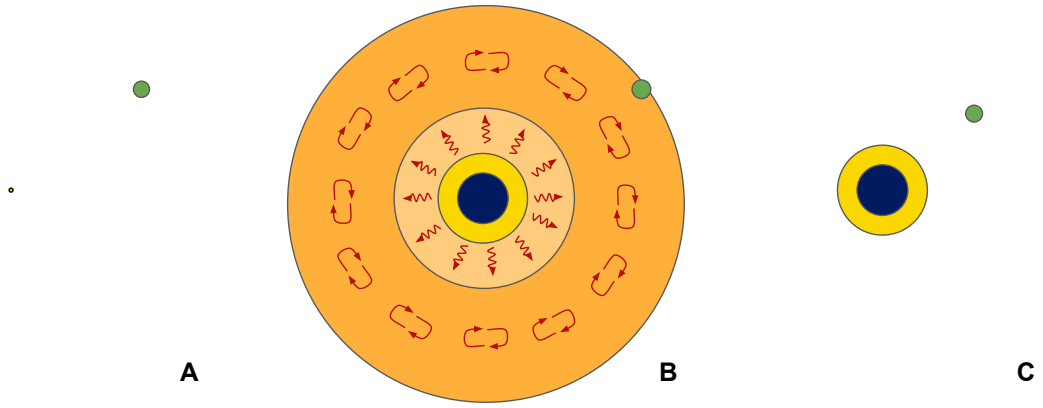

Figure 5: This figure shows the three major steps of CE evolution. **A** illustrates a bound system of a 1 $M_\odot$ MS star and a 0.2 $M_\odot$ companion. The companion in the cartoon is not to scale, as it would not be visible were it shrunk down to 40% the size of the MS star. But the primary, 1 $M_\odot$ MS star is scaled according to **B**'s primary, which is the same star but at its maximum radius as a RGB star (like the largest star in Figure 4). In **B**, the companion has just been engulfed due to the primary's expansion, marking the beginning of a CE event. In **C**, the companion has already spiraled through the primary's envelope and contributed enough energy so that the envelope could be ejected, leaving behind only its degenerate core.

This process is illustrated in Figure 5. Figure 5**A** illustrates a bound system of a 1 $M_\odot$ MS star and a 0.2 $M_\odot$ companion. A 0.2 $M_\odot$ companion would be a brown dwarf, which is a substellar source that is not large enough to sustain hydrogen burning on its own. The companion in the cartoon is not to scale, as it would not be visible were it shrunk down to 40% the size of the MS star, but the primary, 1 $M_\odot$ MS star is scaled according to Figure 5**B**'s primary, which is the same star but at its maximum radius as a RGB star (like the largest star in Figure 4).

Figure 5**B** shows the moment where the primary star, in expanding to its maximum radius, has engulfed the secondary mass in its envelope, marking the first step of a CE event. As will be explained in 2.2.2, it is important to note that the first large zone the companion will encounter in the RGB star is the convective zone. The secondary mass will begin to orbit in the envelope towards the primary star's dense core. Due to the drag force this orbit will rapidly shrink, creating a tight spiral inwards, and the energy released in this process will eventually aid in unbinding the primary star's envelope.

In Figure 5**C**, the companion has transferred enough energy for the primary's envelope to

become unbound and eject from the system. This means that, of the primary star, only the core remains and the overall result is a close binary. There is another option for Figure 5**C** that is not depicted. As the companion moves through the primary's envelope, the drag force will shrink its orbit and slow its motion. If the companion mass is destroyed (called shredded) by the effects of this force before it can transfer enough energy to unbind the envelope, the primary star will remain as is, although the energy that was contributed from the companion may result in a change in its evolutionary track (Nordhaus *et al.* (2011)). Other effects that could change a CE process outcome include mass ratio, initial orbital separation, and internal properties of the giant star (e.g., Marco *et al.* (2011); Politano & Weiler (2007); Zorotovic *et al.* (2011)). For some visualizations of the outcomes of different CE events, see Figure (6).

2.2 Previous Theoretical Work on CEs

The conditions that allow for envelope ejection are dependent on the physics of the interaction, the structure of the envelope, and the details of energy and angular momentum transport during the CE phase (Icko & Livio (1993)). One of the most commonly-used, necessary conditions is that the energy released from the orbit must surpass the binding energy of the envelope. This is denoted as:

$$E_{\rm bind} \leq \bar{\alpha}_{eff} \Delta E_{\rm orb}, \tag{2.1}$$

where $\Delta E_{\rm orb}$ is the orbital energy released during inspiral, $E_{\rm bind}$ is the energy required to unbind the envelope, and $0 \leq \bar{\alpha}_{eff} \leq 1$ is the efficiency with which the liberated orbital energy can be used to unbind the CE (for more information on this see Tutukov & Yungelson (1979); Iben & Tutukov (1984); Webbink (1984); Livio & Soker (1988); Marco *et al.* (2011)). How efficiently this energy can be accessed to drive envelope ejection, and whether this condition is sufficient, is a subject of active research (Ivanova *et al.* (2015); Nandez *et al.* (2015); Chamandy *et al.* (2018a); Grichener *et al.* (2018); Ivanova (2018); Soker *et al.* (2018); Wilson & Nordhaus (2019); Wilson & Nordhaus (2020)).

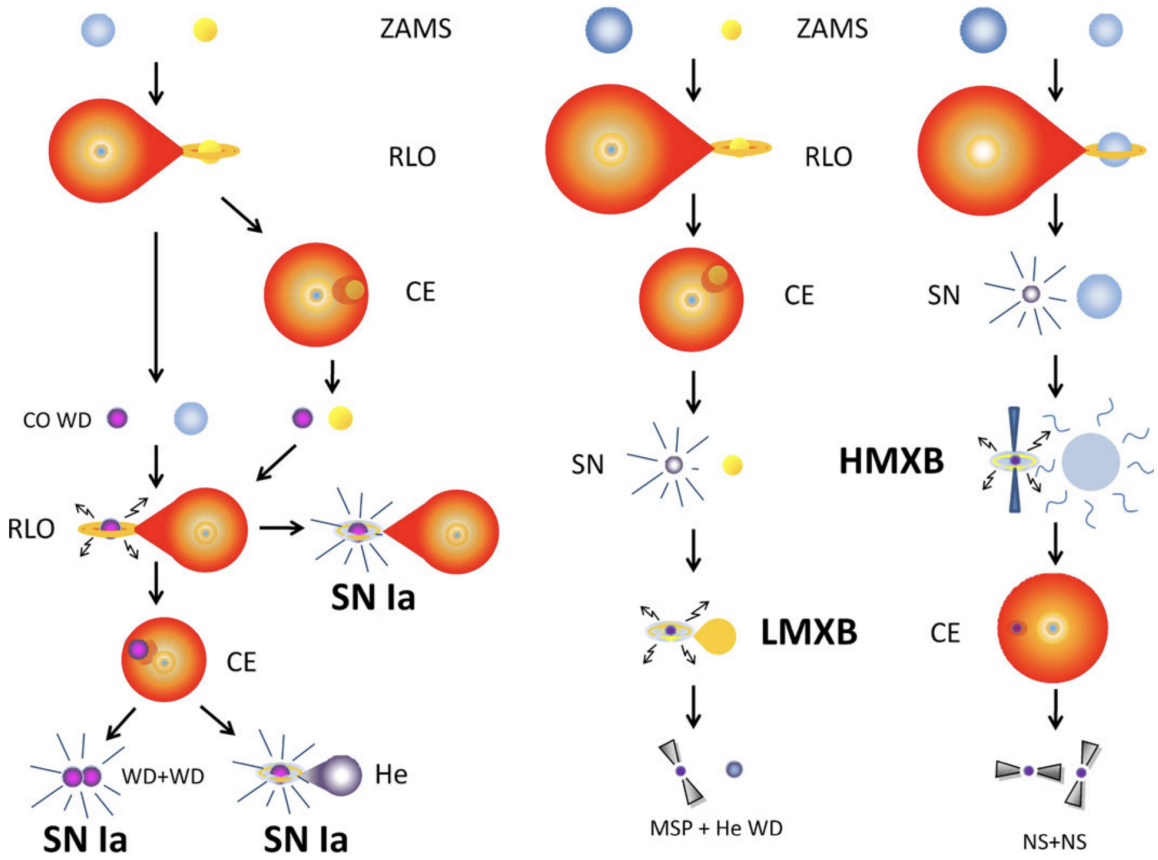

Figure 6: Outcomes of possible CE events as described by Ivanova *et al.* (2012). Each column describes a different means of producing a compact object binary system. The leftmost column has two means of reaching a Type Ia SN event. The center column produces a milli-second pulsar (MSP) and white dwarf (WD) binary. And the rightmost column produces a neutron star-neutron star close binary, which could go on to merge and produce gravitational waves such as the ones observed by LIGO. These are only a few examples of possible outcomes and by no means exhaustive.

2.2.1 Issues with Modeling Theory

Thus far there have been two approaches to understanding CE events: population synthesis studies and numerical simulations. Population synthesis studies of low-mass binaries often use a predetermined constant to define $\bar{\alpha}_{eff}$, and, in order to reproduce observations, this value is often assumed to be low ($\bar{\alpha}_{eff} < 0.1$) (Politano & Weiler (2007); Davis *et al.* (2009); Zorotovic *et al.* (2010); Toonen *et al.* (2017)). But even with this assigned $\bar{\alpha}_{eff}$ value, population studies over-produce long-period binary systems when compared to observational data.

Many numerical simulations of CEs have difficulty completely unbinding the envelope in both low-mass and high-mass CE events. The envelope either remains bound or is only partially ejected when only orbital energy is considered (Ricker & Taam (2012); Passy *et al.* (2011); Ohlmann *et al.* (2015); Chamandy *et al.* (2018a)). To resolve this, many studies have been done to investigate utilizing additional energy sources that would allow the system to reach its required energy limit, such as from accretion, jets or recombination, as well as from processes on longer timescales (Ricker & Taam (2008); Ivanova *et al.* (2015); Nandez *et al.* (2015); Soker (2015); Kuruwita *et al.* (2016); Sabach *et al.* (2017); Glanz & Perets (2018); Grichener *et al.* (2018); Ivanova (2018); Kashi & Soker (2018); Soker *et al.* (2018); Reichardt *et al.* (2020); Schreier *et al.* (2021); Lau *et al.* (2022)).

While these effects are useful to consider, it may first be helpful to consider the physical effects incorporated in simulations. The amount of energy allowed for unbinding the primary's envelope in a CE interaction is set by the initial orbital energy. As the companion goes through its inspiraling orbit, this liberated orbital energy can be transferred to aid in unbinding unless it is lost via radiation, which is notably not included in hydrodynamic simulations. This means these simulations contain an incomplete analysis of the ejection efficiency $\bar{\alpha}_{eff}$. This is to say a more comprehensive review of the energy components in CE simulations is needed (Chamandy *et al.* (2018b)), but a means of accounting for the liberated orbital energy that escapes the system in particular is certainly required (Wilson & Nordhaus (2019); Wilson & Nordhaus (2020); Wilson & Nordhaus (2022)).

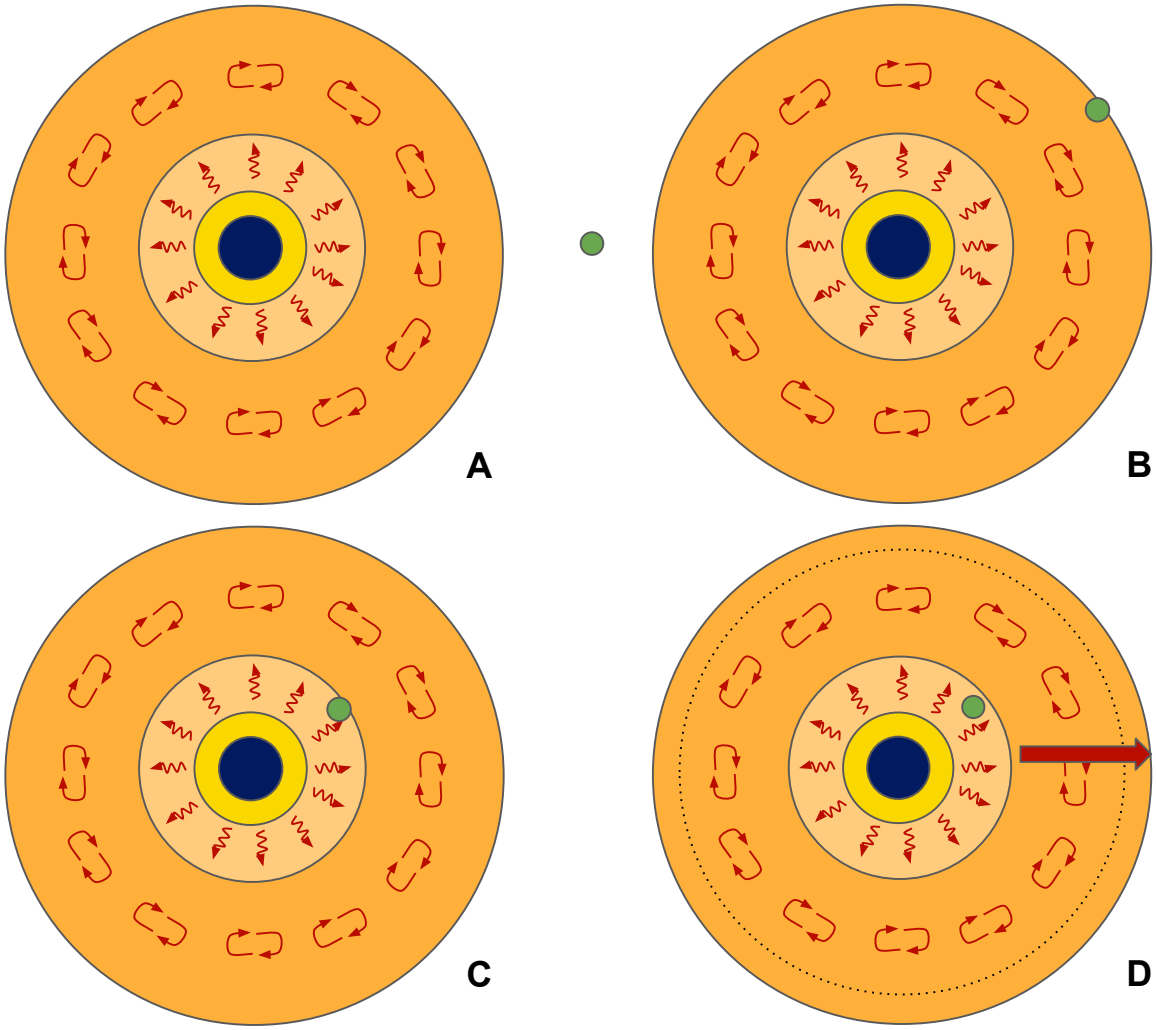

Figure 7: Here are the steps of a Common Envelope (CE) event. **A** shows the primary star at its maximum radial extent, as well as the companion mass in green. Note that the primary star is a RGB star, and the zones are the same as those from Figure 3. **B** represents the first step of a CE event, when the secondary mass has entered the outer edge of the primary star's envelope, specifically the convective zone, which, in low-mass primary stars, closely correlates to the SCCR. In this step it begins its inspiral towards the primary's core. In **C** the companion has entered the radiative zone, which marks the moment where the liberated energy of the companion's orbit is no longer radiated away and instead entirely contributes to envelope ejection. This effect is illustrated in **D** with a red arrow, representing the outward force on the primary's envelope. The dotted circle in **D** represents the previous location of the star's outer bounds from **A**, **B**, and **C**.

2.2.2 Convection is a Necessary Ingredient in CE Evolution

If $\bar{\alpha}_{eff}$ is given, it is possible, with knowledge of the energy required to unbind the primary star's envelope, to predict the post-CE orbital separation of a system. But, as mentioned in Section 2.2, it is precisely how to account for this value that has caused the greatest issues thus far. Population synthesis studies do not find $\bar{\alpha}_{eff}$, but rather define it as one of the principal constants, while numerical simulations seem to ignore radiative effects.

However, using detailed stellar interior profiles, Wilson & Nordhaus (2019) were able to calculate $\bar{\alpha}_{eff}$ for a matrix of primary-companion mass pairs when the primary was at the maximal extent of its evolution. This proved that the ejection efficiency is most sensitive in the surface-contact convective region (SCCR). The SCCR is defined as a zone where the convective transport timescales are shorter than the orbital decay timescales, which allows the star to radiate orbital energy and lower $\bar{\alpha}_{eff}$. Illustrations of this process are shown in Figures 7 and 8. The effect of these convective zones includes predicted post-CE orbital periods of less than a day in many of the primary-companion pairings, which matches observation. Also, so long as the properties of the SCCR are known, $\bar{\alpha}_{eff}$ can be calculated. Specifically, in the SCCR, 0% of the energy produced is allowed to contribute to envelope ejection ($\bar{\alpha}_{eff} = 0$), and, in the non-SCCR, 100% of the energy produced is allowed to contribute to envelope ejection ($\bar{\alpha}_{eff} = 1$).

SCCRs have also successfully replicated double white dwarf (DWD) systems (Wilson & Nordhaus (2020)). Again, by applying these convective effects, the predicted post-CE final separations closely match those in observed DWD orbital parameter strength, another motivation that convection is key in CE evolution. And, although this work only looks at low-mass primary stars, the effects of convection and radiative losses in high-mass CEs also match observations of Wolf-Rayet binary systems (Wilson & Nordhaus (2022)).

The work in understanding the role of convection in CE events through SCCRs has been detailed in previous work (Wilson & Nordhaus (2019); Wilson & Nordhaus (2020); Wilson & Nordhaus (2022)). In this thesis, we explore these effects on the light curves of common envelopes in particular.

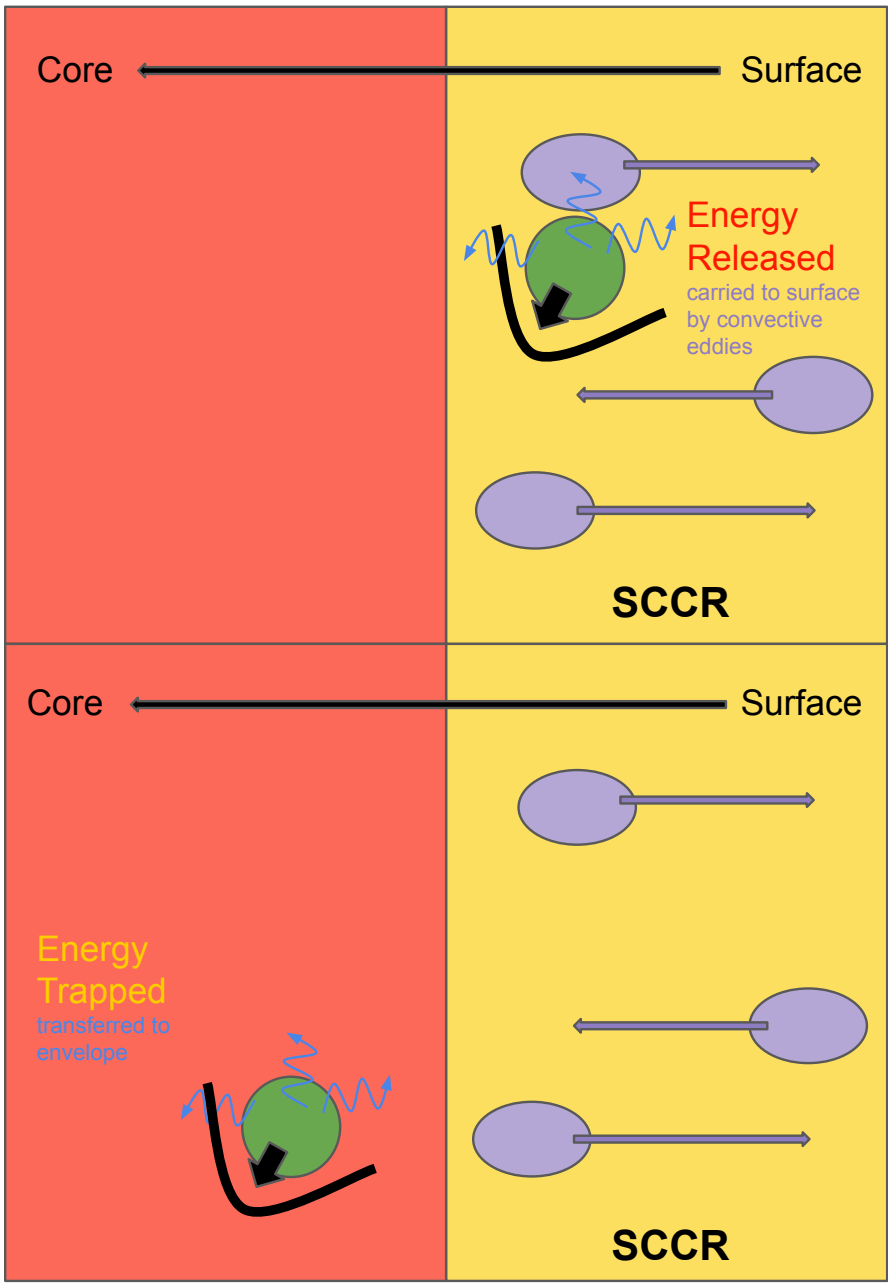

Figure 8: This cartoon illustrates the model of convection introduced in Wilson & Nordhaus (2019) and implemented in this work. The companion, illustrated as a green circle, moves from the surface-contact convective region (SCCR, in yellow) of the primary into the radiative zone of the primary (in red). The black arrow represents the direction of motion of the green companion. The black arch represents the effects of the drag force, while the smaller blue arrows represent the energy released due to the companion's motion. While it is in the SCCR (yellow), the energy can be carried to the surface and out of the star via convective eddies, illustrated via purple ovals. Otherwise, once the companion reaches the radiative zone (red), its energy is entirely contributed to the primary.

3 Common Envelope Theory

As expounded upon in Section 2.2.1, modeling efforts, specifically for numerical simulations, have thus far been ineffective in matching observed post-CE events. Previous work modeling these light curves has either come from post-processing numerical simulations or back-of-the-envelope calculations that assume the envelope ejection occurs rapidly, with the envelope often expanding on a dynamical timescale (Galaviz *et al.* (2017); Ivanova *et al.* (2013)). Again, these numerical simulations often cannot eject the envelope without additional energy sources (Ricker & Taam (2012); Passy *et al.* (2011); Ohlmann *et al.* (2015); Chamandy *et al.* (2018a)). Furthermore, in both cases, important physical effects which are known to occur in giant stars and should influence the outcomes are missing, namely convection and radiation. The exclusion of these effects produce changes in the light curves on the order of several months (Figure 17).

Despite these issues, attempts to match incomplete models to observational data has been made (Iaconi & de Marco (2019)), and a modeled light curve has even been proposed and matched to a possible source (Ivanova *et al.* (2013)). However, the source, and whether it is truly a CE, merger, or mass loss episode, is the subject of debate (Kashi & Soker (2016)). So the search for modeled light curves that predict and definitively match CE evolution sources is still well underway (Hatfull *et al.* (2021)). This work fundamentally differs from previous modeling efforts, as it includes the effects of convection and radiative cooling, which have been determined to be important to CE evolution (Wilson & Nordhaus (2019); Wilson & Nordhaus (2020); Wilson & Nordhaus (2022)). It also proves, in Section 4.3, that these effects impart a quantitatively distinct signature on timescales of years to decades.

3.1 Stellar Interior Models

Investigating the outcomes of stellar evolution requires models for the interiors of giant stars at the onset of the CE phase. To generate these models, we employ the open-source stellar evolution code MESA (release 10108; Paxton *et al.* 2011, 2018). MESA produces spherically symmetric models of stellar interiors at discrete times in the star's evolution. Each model was

evolved from the pre-Main-Sequence (PMS) to the White Dwarf (WD) phase for Zero Age Main-Sequence (ZAMS) masses.

Models were generated for stellar masses of 1 $M_\odot$, 2 $M_\odot$, and 3 $M_\odot$, and evolved in increments of 0.2 $M_\odot$ with solar metallicity (z = 0.02). Mass-loss on the Red Giant Branch (RGB) followed a Reimer's prescription with $\eta_R = 0.7$, while mass-loss on the Asymptotic Giant Branch (AGB) followed a Blöcker prescription with $\eta_B = 0.7$ (Reimers (1975); Bloecker (1995)). Figure 9 illustrates how the size of each of the primary masses changed over time in the MESA profiles.

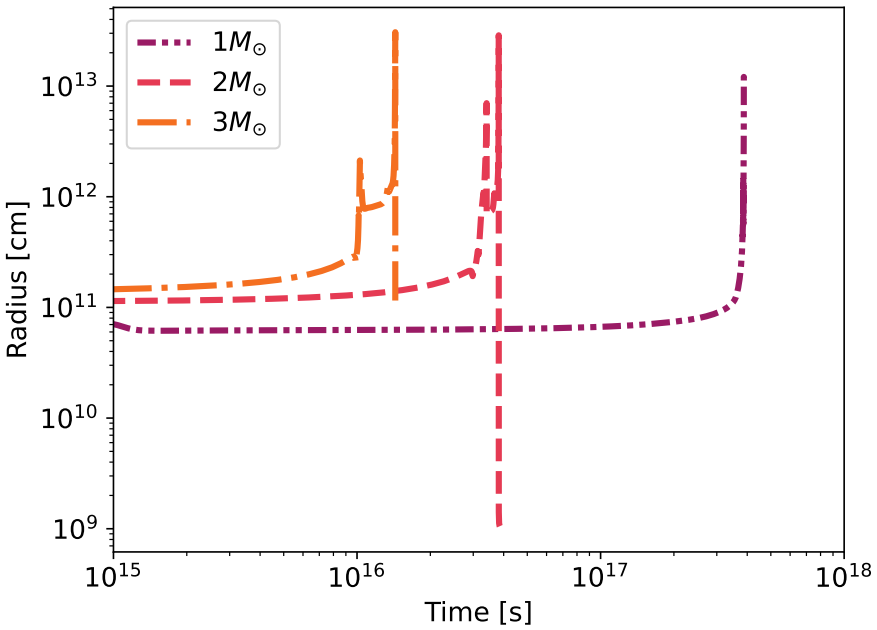

Figure 9: Illustrated here is the outermost radius of the stars evolving over time for the 1 $M_\odot$, 2 $M_\odot$, and 3 $M_\odot$ models from MESA. In order for the most likely case where a companion would be engulfed, the largest radius in time for each profile was chosen, in other words the maximum y-value for each of these curves. Note that in the 1 $M_\odot$ this occurs while the star is on the RGB (1.1.3), but for the 2 $M_\odot$ and 3 $M_\odot$ cases the star is on the AGB (1.1.4).

For each evolutionary model, the point in time where the star has attained its maximum radius was chosen. This yields the largest cross section for CE interactions, making it a likely time for a CE event to occur, as the primary occupies its greatest possible volume for engulfing its companions. This large size also results in strong tidal torques that will shrink the orbit

of companions that avoid direct engulfment but are orbiting within ∼10 AU (Nordhaus & Spiegel 2013; Nordhaus *et al.* 2010; Villaver & Livio 2009). For each star, the MESA interior profile includes radial information regarding the mass, density, convective properties, and core and envelope boundaries. For example, the interior temperature of a 1 $M_\odot$ (purple), 2 $M_\odot$ (pink), and 3 $M_\odot$ (orange) star as a function of radial position inside the star is plotted in Figure 10. Radial information such as this is then used to calculate the primary star's binding energy, location of the convective zones, inspiral timescales, tidal disruption radii, and the energy released during orbital decay.

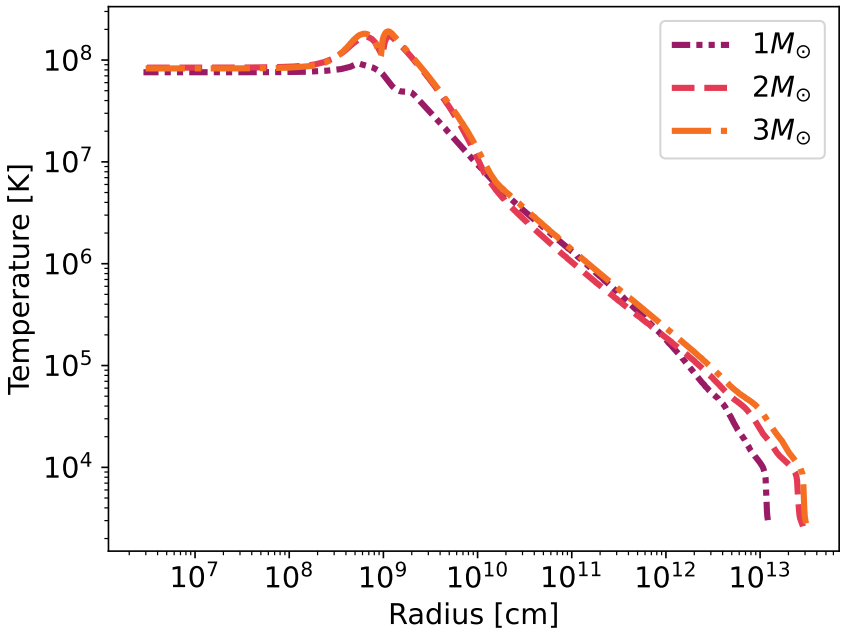

Figure 10: This figure shows how the interior of each of the primary stars at their maximum radius values (Figure 9) changes with temperature. The purple dash-double dot curve shows the 1 $M_\odot$ model, while the red dashed curve and orange dash-dot curve show the 2 $M_\odot$ and 3 $M_\odot$ models respectively. The x-axis is from the core of the star to the edge, and the y-axis is from cool to hot temperatures.

The calculations that follow allow the CE efficiency to be determined, as well as the post-CE orbital separations for the companions that survive the CE interaction. Additionally, the time-evolution of the luminosity during CE evolution can be calculated. From this, one can produce light curves that in turn can be used to calculate the predicted fluxes and magnitudes

of these events. Such theoretical time-domain signatures will be important for upcoming transient facilities, such as the Vera C. Rubin observatory (Željko Ivezić *et al.* (2008)).

3.2 Orbital Decay and Envelope Ejection

To identify the first, convective region of the primary star, the calculated convective velocities (v_{conv}) from MESA are extracted from the interior profile when the star is at the maximum radial extent in its evolution. This allows for calculating the convective timescale, as shown in eqn. 3.2. This is the time required for convection to carry energy from the point r in the primary star out to the primary's surface ($R_\star$).

$$t_{conv}[r] = \int_r^{R_\star} \frac{1}{v_{conv}[r]}\,\mathrm{d}r \tag{3.2}$$

Note that terms shown with an r in square brackets are radially dependent. Through a similar method we can determine, for each radial point in the primary, the time required for the orbit to fully decay, otherwise known as the inspiral timescale (Nordhaus & Blackman (2006)). This is given as,

$$t_{inspiral}[r] = \int_{r_i}^{r_{shred}} \frac{(\frac{\mathrm{d}M}{\mathrm{d}r} - \frac{M[r]}{r})\sqrt{v_r^2 + (\bar{v}_\phi[r]^2 + c_s[r]^2)^2}}{4\xi\pi G m_2 r \rho[r]}\,\mathrm{d}r, \tag{3.3}$$

where r_i is the initial radial position, r_{shred} is the tidal shredding radius, which can be estimated via $r_{shred} \approx R_2 \sqrt[3]{\frac{2M_{core}}{m_2}}$ (where M_{core} is the mass of the core of the primary star and m_2 is the mass of the companion), $c_s[r]$ is the speed of sound at each radial position in the star, and $\bar{v}_\phi = v_\phi - v_{env} \approx v_\phi$ for slow rotators such as RGB/AGB stars (Nordhaus *et al.* (2007)). Additionally, the parameter ξ, accounts for the geometry of the companion's wake, the gaseous drag of the medium, and the Mach number (Park & Bogdanović (2017)). Here, it is assumed $\xi = 4$. We note that the ejection efficiency $\bar{\alpha}_{eff}$ is not sensitive to this parameter (ξ) for the mass ratios considered here.

These two timescales are illustrated in Figure 11, which includes a graph for each of the three primary masses. The convective timescale, the time required at each position along the

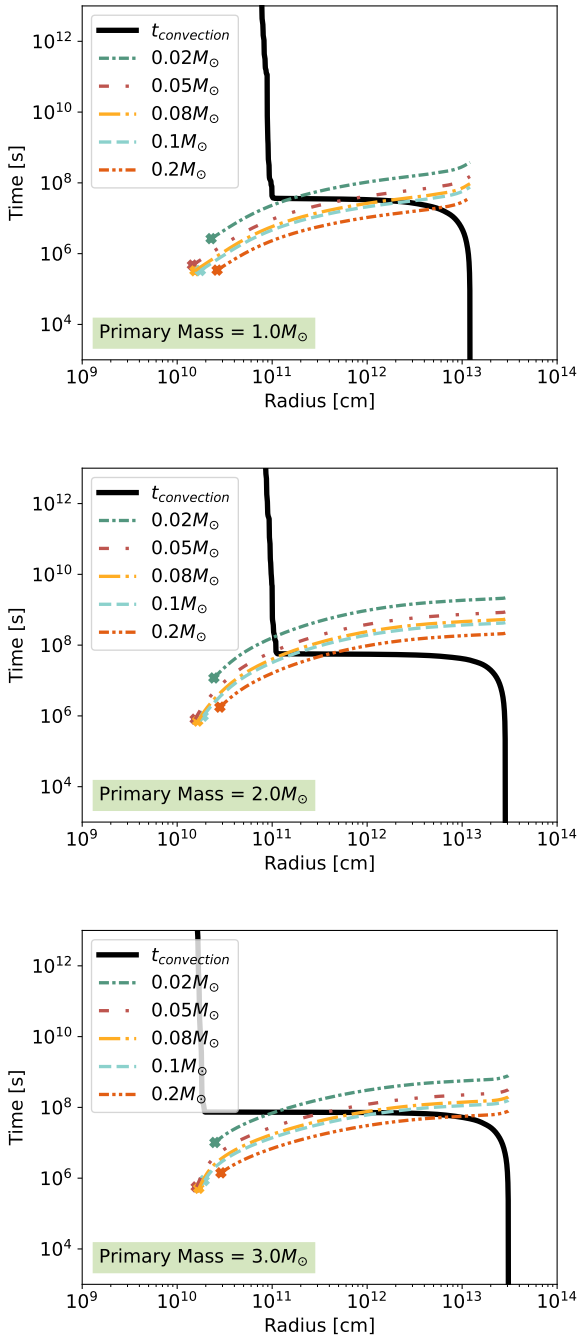

Figure 11: Illustrated above are the inspiral and convective timescales for primary masses from 1 $M_\odot$ (at the top) to 3 $M_\odot$ (at the bottom). The convective timescales, the time required for convection to carry energy from point r in the primary star out to the primary's surface ($R_\star$), are shown by a thick, black line. The inspiral timescales (the time required for the companion mass to spiral from its current radius to the center of the primary star) for the five companion masses are illustrated with different colors and line styles. The shredding radius, where the companion mass shreds due to the primary star's gravity, for each companion is marked with an "X."

primary star's radius for energy to be carried from that point to the star's surface, is shown in black. The inspiral timescales, the time required for the companion mass to spiral from its current radius to the center of the primary, of several masses are also shown using various colors and line patterns. These lines end at the point where they would shred due to the primary's gravitational force, marked by an "X". If the envelope is ejected before this point the secondary mass will survive, as the process will halt before it reaches the shredding radius, and the remnant will be a close binary.

In regions where $t_{conv} \ll t_{inspiral}$, convection will transport orbital energy radially outward faster then the orbit decays. This energy will reach the optically thin surface region where it is radiated away. For lower-mass stars ($\lesssim 3$ $M_\odot$) there tends to be only a single convective region at maximum extent, whereas stars larger than this have a deeper, yet physically distinct, secondary convective layer (Wilson & Nordhaus (2019)). All the models used here only have a single SCCR zone.

3.2.1 Energy and Luminosity Considerations

In order to compute $\bar{\alpha}_{eff}$, the energy required to unbind the primary's envelope must be known. Using direct calculations from the MESA stellar evolution models, it is possible to avoid adding in parameters that approximate the primary star's gravitational binding energy for situations where the interior structure is not known (Marco *et al.* (2011)). Then, the minimum energy required to eject the envelope's mass exterior to a radius r is given by:

$$E_{bind}[r] = -\int_{M}^{M_\star} \frac{GM[r]}{r}\,\mathrm{d}m[r], \tag{3.4}$$

where $M_\star$ is the total mass of the primary star. This is often referred to as the binding energy of the envelope.

The energy liberated via inspiral is:

$$\Delta E_{orb}[r] = \frac{Gm_2}{2}\left(\frac{M[r_i]}{r_i} - \frac{M[r]}{r}\right), \tag{3.5}$$

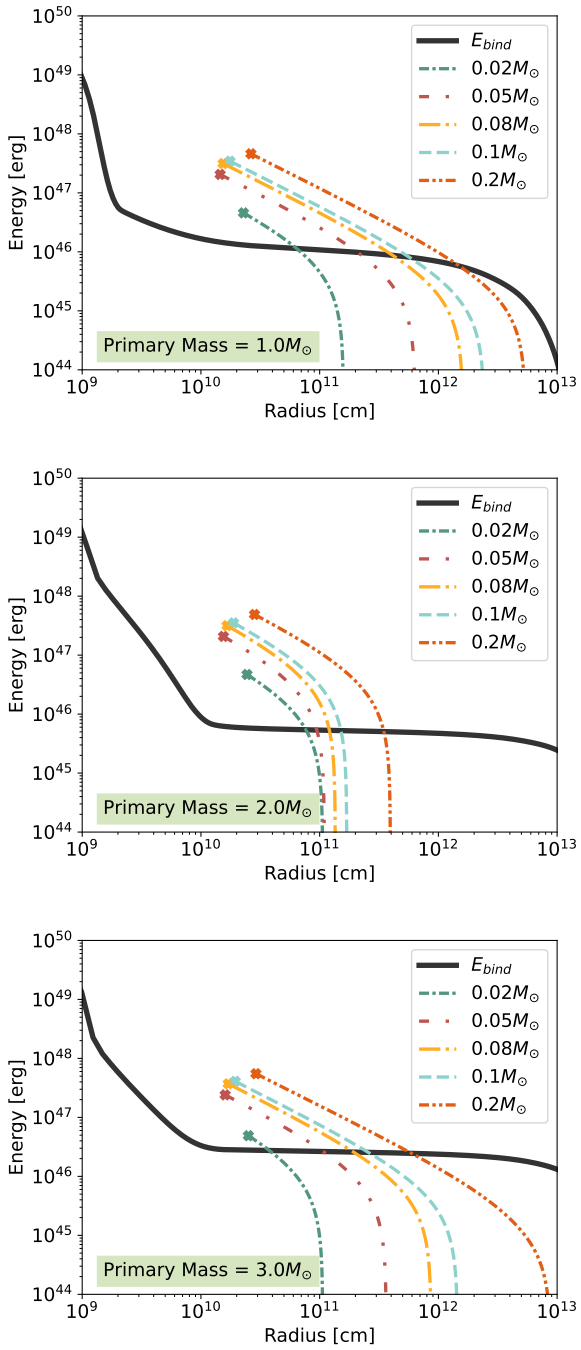

Figure 12: Illustrated above are the inspiral and binding energies for the three primary masses, from 1 $M_\odot$ (at the top) to 3 $M_\odot$ (at the bottom). The binding energy, in black, at every point in the primary star's radius represents the minimum amount of energy the star requires for its envelope to unbind. The companion's inspiral energies, shown in different colors and line patterns, all intersect with the binding energy before ending with an "X." The "X's" represent the shredding radius for each companion, and, because these occur after intersection, they all unbind the primary's envelope and survive to form close binary pairs.

where r_i is the radius of the companion's orbit at the onset of energy transfer due to its inspiral through the primary star.

In Figure 12, the binding and inspiral energies for the three primary stellar masses and their respective companion masses are shown. For this work, only companion masses whose inspiral energy values intersected the binding energy (in black) were used, as these represent companions that meet the minimum energy requirement necessary to unbind the primary star's envelope without being shredded (shown by an "X"). This means the point of crossover between these two energy lines is approximately the final separation of the binary. For work that investigates shredded companion effects, see Yarza *et al.* (2022).

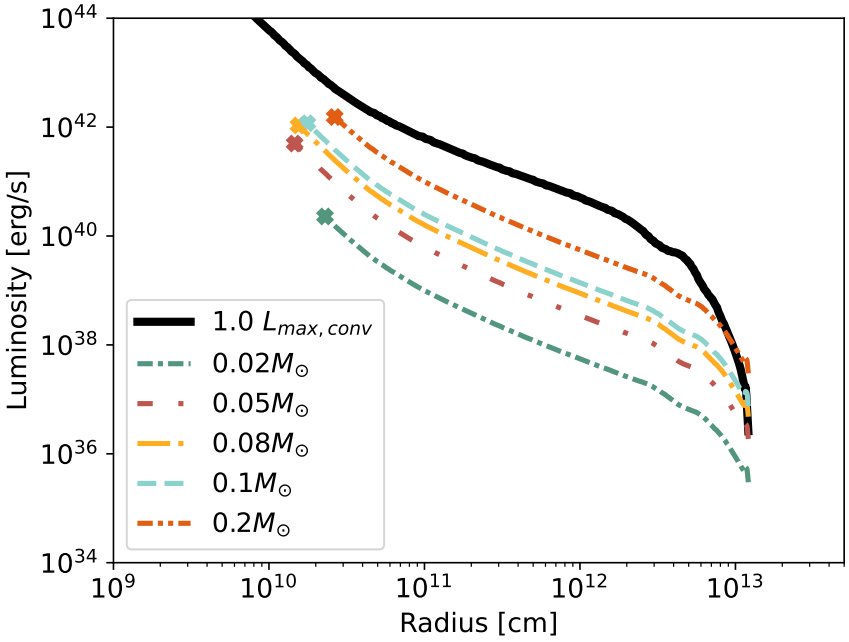

Figure 13: The maximum luminosity convection can carry out of the 1 $M_\odot$ primary star is shown by the solid black line labeled $L_{max,conv}$. The drag luminosities for several companions are shown with the dashed and coloured lines. The radii points where the companions are destroyed via tidal disruption are marked by an "X." Altogether, this figure shows what amount of orbital energy from the companions, in the form of luminosity, can be carried to the surface of the star via convection and radiated away. Note that, for the modeled light curves, the companions all meet the binding energy minimum, illustrated in Figure 12, before they meet the tidal disruption radii. Therefore they will be stopped by the ensuing envelope ejection force before they are destroyed by the primary.

From eqn. 3.4 and 3.5, the ejection efficiency parameter $\bar{\alpha}_{eff}$ can be derived as:

$$E_{\text{bind}} = \bar{\alpha}_{eff} \Delta E_{\text{orb}}. \tag{3.6}$$

Again, $\bar{\alpha}_{eff}$ is the effective efficiency of energy transfer to unbind the envelope from the decaying orbit of the companion. If $\bar{\alpha}_{eff} = 1$, then the process is 100% efficient and all the orbital energy goes towards unbinding the envelope of the primary. If $\bar{\alpha}_{eff} = 0$, then the process is 0% efficient and all the orbital energy leaves the system, meaning the CE will never be ejected. As in Wilson & Nordhaus (2019), $\bar{\alpha}_{eff}$ is set to 0 for regions of SCCR and 1 for regions of non-SCCR.

The drag luminosity, generated from the inspiral orbit of the companion, is given as:

$$L_{drag} = \xi \pi r_{acc}^2 \rho[r] v_\phi^3[r], \tag{3.7}$$

where $r_{acc} = \frac{2Gm_2}{v_\phi^2[r]}$ is the accretion radius (Nordhaus & Blackman (2006)). The drag luminosities of several different companion masses at each radial position in a 1 $M_\odot$ primary star can be seen in Figure 13.

This drag luminosity can also be derived as a function of time using the inspiral timescale, so that the change in luminosity of the system can be observed as the CE event moves forward in time (Figure 14). This is the first step in producing an overall light curve, as the resulting graph illustrates how the star's luminosity is affected from the moment the CE event begins until the companion moves into the non-SCCR region and its energy starts contributing to unbinding the envelope. From this point, the star will undergo a process similar to a Type II SN event (1.1.6), as the envelope is blown off and the degenerate core is left behind.

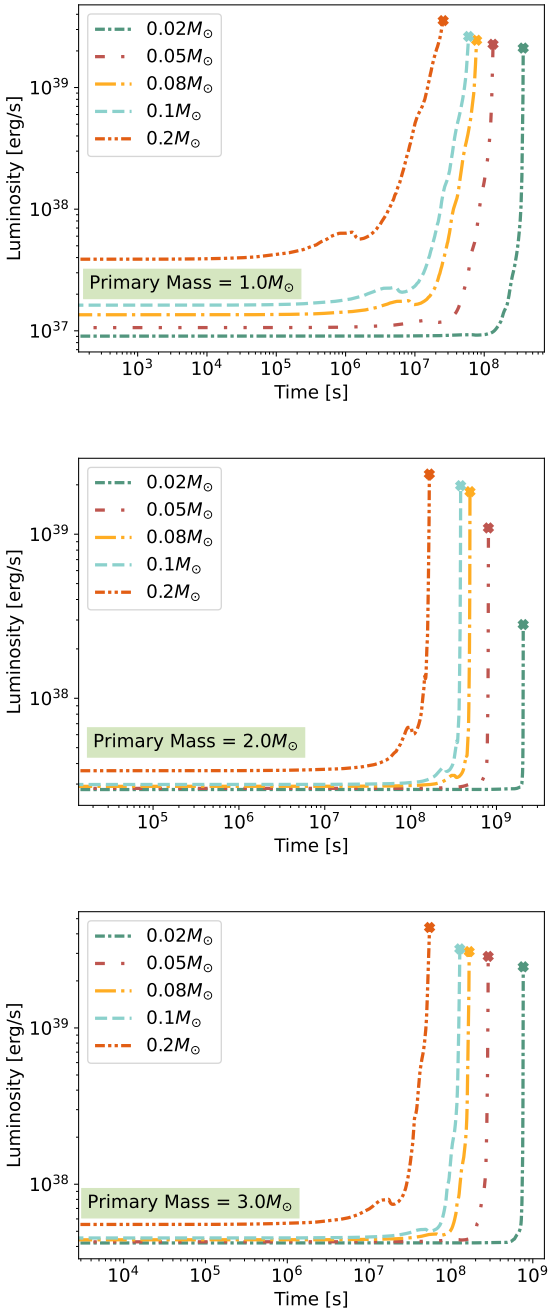

Figure 14: The drag luminosities that would be visible as the companion enters the SCCR zone of the primary star, where the orbital energy can be carried out of the star and radiated away, is shown here for the three primary masses and each of the five companion masses over time. The points where each companion moves from the SCCR to the non-SCCR region of the star is shown with an "X." Beyond that point, the energy of the companion is kept entirely within the star and used to unbind the envelope of the primary, therefore none is able to escape as luminosity. So the system's overall luminosity at that point is no longer effected by the companion's inspiraling orbit.

4 Common Envelope Light Curves

Figure 14 shows the drag luminosity that reaches the surface during the common envelope inspiral phase. Once the orbital energy can no longer be transported to the surface, the energy must contribute to unbinding the envelope. If this is greater than the binding energy of the envelope, the primary star's envelope is ejected. The lightcurve for the ejection phase is then similar to that of a Type IIP SN (1.1.6), characterized by a unique plateau (P) in their light curves, which have been studied with great detail (Chugai (1991); Popov (1993); Kasen & Woosley (2009)). The application of Type IIP SN luminosity to a CE event for this stage has already been made in other light curve modeling efforts (Ivanova *et al.* (2013); Hatfull *et al.* (2021)).

4.1 The Plateau Phase

In the Type IIP SN model, the stellar plasma expands and cools as it is pushed outward in the ejection process. Recombination, defined here as ions recombining into hydrogen atoms, due to this cooling then changes the plasma's opacity, which propagates a "cooling wave," or recombination front, through the star, as illustrated in Figure 15. The location of the recombination front stays relatively constant, producing a visible plateau. This is called the plateau phase.

To calculate the luminosity change in this phase of the system, the work of Popov (1993) was used, which presents an analytical model for the plateau stage of Type IIP SN. The observable feature of the SN light curve includes the duration of the plateau (t_p). This can be expressed using the energy of the ejection and the ejected mass, as well as the initial radius of the envelope. Analytical models are useful because they can provide general parameters for an event, such a SN, without the complexities of numerical computations.

4.1.1 Derivation

The main assumptions of this model include a uniform density profile,

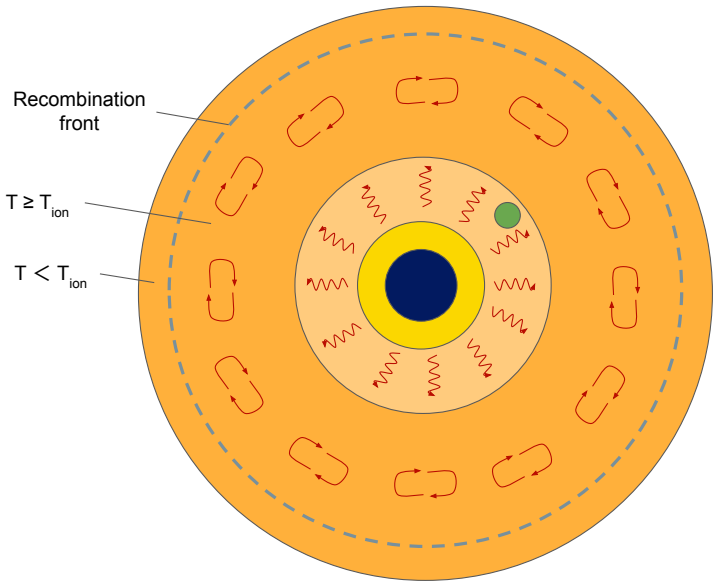

Figure 15: This figure shows the bounds of the recombination front when the red giant is at its largest size. The surface temperature of a red giant is close to 3000 K, whereas recombination occurs between 5000-6000 K. Therefore, the recombination boundary is found inside the envelope. This also marks the bounds, according to Popov, between the opaque and transparent parts of the envelope, with the envelope being transparent between the surface of the star to the outer edge of the recombination front before becoming opaque.

$$\rho(x,t) = \rho_0 \frac{R_0^3}{R(t)^3}, \tag{4.8}$$

and approximate opacity via a step function of temperature, assuming at a specific temperature T_{ion} that the recombination of hydrogen occurs:

$$\kappa_t(x,t) = \begin{cases} \kappa, & \text{if } T \geq T_{ion} \\ 0, & \text{if } T < T_{ion}. \end{cases} \tag{4.9}$$

This creates a "two-zone" model where, at temperatures inside the envelope that are greater than T_{ion}, the envelope is opaque and, at temperatures less than T_{ion}, the envelope is transparent. The boundary between is called the recombination front. The moment recombination begins is denoted by time t_i, and the radius where this boundary between the opaque and transparent zones is located is denoted by R_i (this is illustrated in Figure 15).

The characteristic timescales for this model are the photon diffusion timescale,

$$t_d = \frac{9\kappa M}{(4\pi^3 c R_0)}, \tag{4.10}$$

and the expansion timescale,

$$t_e = \frac{R_0}{v_{sc}}. \tag{4.11}$$

The envelope kinetic energy is $E_{kin} \approx E$, the total energy of the ejection. An approximated scale velocity can be derived in the case of uniform density as eqn. 4.12.

$$v_{sc} = \sqrt{\frac{10E}{3M}} \tag{4.12}$$

We also define a characteristic time, t_a, for the changes in the magnitude in models given by:

$$t_a = \sqrt{2 t_d t_e}. \tag{4.13}$$

In the plateau phase, recombination begins at moment t_i, where the surface temperature of the gas reaches T_{ion}. The value of t_i is calculated from eqn. 4.19, which is derived from the two luminosity equations below (eqn. 4.15 and 4.18).

Combining the previously derived terms, one can find the radius of the photosphere of the envelope (eqn. 4.14). The photosphere is the lowest layer of a star's atmosphere, or the innermost point that can be observed directly, e.g. is optically thin enough to allow energy, and therefore luminosity, to escape from the system.

$$R_i(t)^2 = v_{sc}[t_i t(1 + \frac{t_i^2}{3t_a^2}) - \frac{t^4}{3t_a^2}] \tag{4.14}$$

Because the photosphere gives the bounds for where light can escape from the system, one can then calculate the luminosity, as in eqn. 4.15.

$$L_{bol}(t) = 8\pi\sigma_{SB} T_{ion}^4 v_{sc}^2 [t_i t(1 + \frac{t_i^2}{3t_a^2}) - \frac{t^4}{3t_a^2}] \tag{4.15}$$

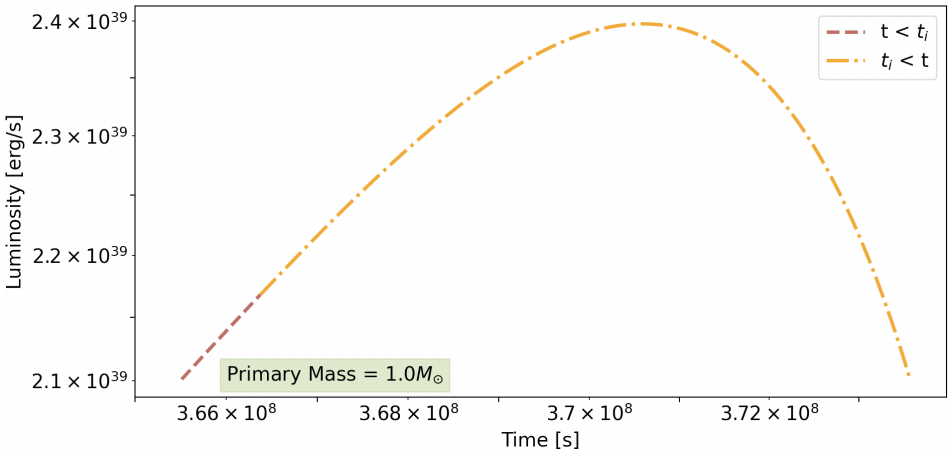

Figure 16: Illustrated here is a light curve of only the plateau phase for a primary mass of 1 $M_\odot$ and a companion mass of 0.02 $M_\odot$. The differently colored sections represent the zones where $t < t_i$ and $t > t_i$, where t_i is when the surface temperature of the star reaches T_{ion}.

Here, σ_{SB} is the Stefan-Boltzmann constant. The maximum bolometric luminosity will occur at time t_m shown below.

$$t_m = [\frac{3}{4} t_i t_a^2 (1 + \frac{t_i^2}{3t_a^2})]^{\frac{1}{3}} \tag{4.16}$$

The duration of the plateau, t_p, can be estimated by setting $R_i(t_p) = 0$ in eqn. 4.14 and solving for t_p:

$$t_p = [3 t_i t_a^2 (1 + \frac{t_i^2}{3t_a^2})]^{\frac{1}{3}} = 4^{\frac{1}{3}} t_m. \tag{4.17}$$

For $t < t_i$, the surface temperature of the envelope is greater than T_{ion}. This means the constant opacity models of Arnett (1980) can be used to estimate t_i. The bolometric luminosity for $t < t_i$ under these assumptions can be defined as:

$$L_{bol}(t) = \frac{E_{th}(0)}{t_d} e^{-\frac{t^2}{t_a^2}}. \tag{4.18}$$

Time t_i can be found by setting both luminosity equations on either side of the recombination front (eqn. 4.15 and 4.18) equal, as show in eqn. 4.19.

$$\frac{E_{th}(0)}{t_d} e^{-\frac{t_i^2}{t_a^2}} = 8\pi\sigma_{SB} v_{sc}^2 t_i^2 T_{ion}^4 \tag{4.19}$$

Figure 16 illustrates these two luminosities with the boundary between the two at t_i.

4.2 The Post-Plateau Phase

After this plateau phase, the luminosity drops rapidly by several orders of magnitude, as only the degenerate remnant is left behind. Therefore, the end of the light curve is an extension of this rapid decay. In this work, this section was an interpolated extension of the declining trend from the end of the plateau phase.

An example full light curve of a common envelope system consisting of a 1 $M_\odot$ primary star and 0.2 $M_\odot$ secondary companion can be seen in Figure 17 in blue-green. Also shown in comparison is a modeled light curve from Hatfull *et al.* (2021) that does not include the effects of convection or radiative cooling. When convection is included, the light curve exhibits a clear increase over the duration of three decades. When convection is not included, the light curve is substantially different, exhibiting change on a much shorter timescale (on the order of a hundred days).

4.3 Light Curves

Figure 18 includes models of 1 $M_\odot$, 2 $M_\odot$, and 3 $M_\odot$ primary stars with companions of between 0.02 - 0.2 $M_\odot$. These secondary masses were chosen because they allowed for enough energy to unbind the envelope without being shredded, therefore making them good candidates to form close binary systems.

The three different phases of calculations have been put together to form the full light curves. They begin with the inspiral through a convective CE, as described in Chapter 3. This phase encapsulates approximately the first decade of the light curve. Next is the plateau phase (driven by the expanding envelope), as outlined in Section 4.1. This phase lasts on the order of approximately 100 days, and occurs far more quickly than the CE section of the light curve (this is why surveys like that of the Vera C. Rubin observatory are important; they

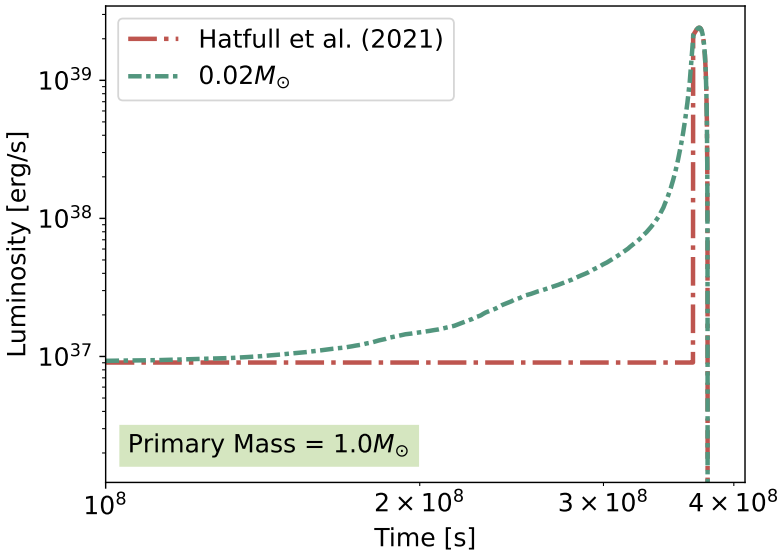

Figure 17: Here is an example of a full light curve in blue-green and dash-dotted line style for primary mass 1 $M_\odot$ and companion mass 0.02 $M_\odot$. Also pictures is an example light curve from the models described in Hatfull *et al.* (2021), which do not include convection and radiative cooling.

will observe the sky with enough frequency to capture a quick event such as this). The final phase of the model light curves, described in Section 4.2 and occurring over approximately two decades, is the luminosity drop off. This is due to the envelope leaving the system and the emergence of the white dwarf.

4.4 Intermediate-Luminosity Optical Transients (ILOTs)

Intermediate-luminosity optical transients, or ILOTs, are defined as events with luminosities between novae and peak SN events, or, more specifically, luminosities about four orders of magnitude above those of novae (Soker & Kashi (2011)). This means their total explosion energies are approximately between $10^{46} - 10^{49}$ erg, and, as Figure 12 demonstrates, this is precisely the range of the CE events calculated in this work. Along with these intermediary luminosity values, ILOTs are defined to last for a time period of weeks to several years, result from a binary interaction, and have an expansion velocity of several hundreds of kilometers per second. The events of Figure 18 meet these various requirements, and therefore it could

be that as yet undefined ILOT events could be a result of convective CE evolution.

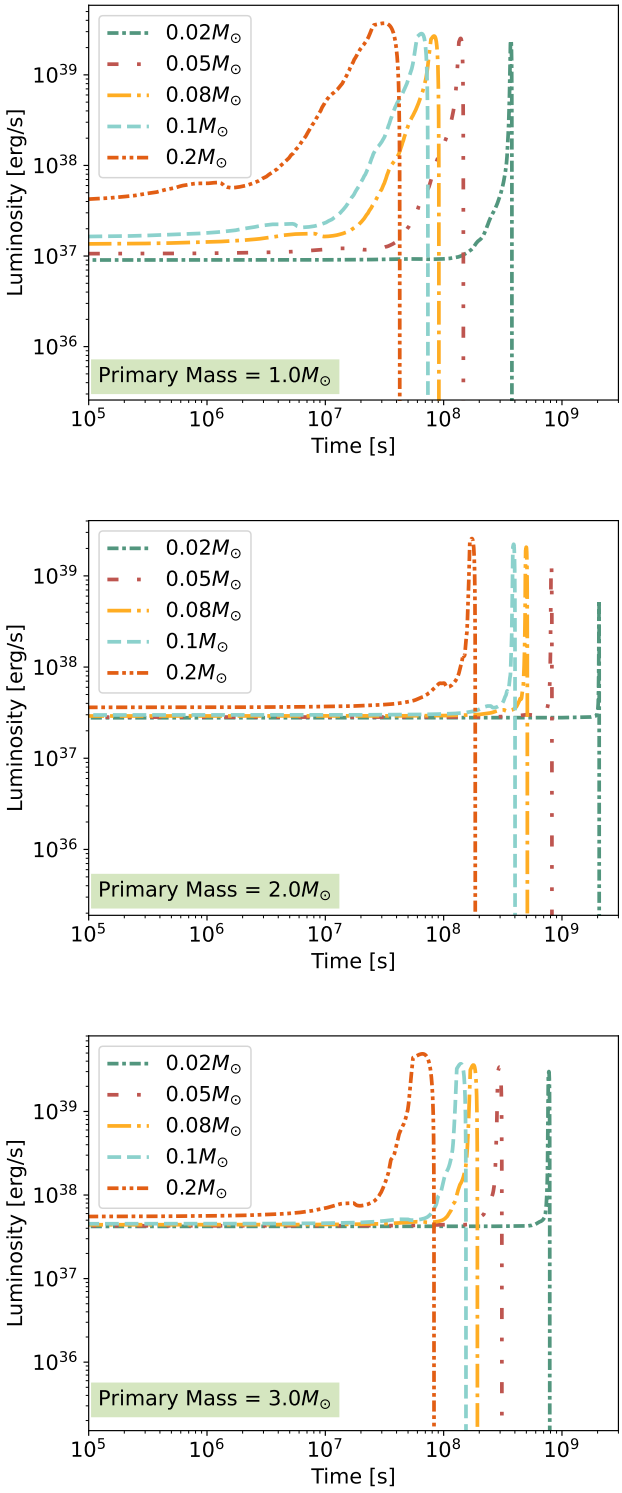

Figure 18: The complete light curves for primary masses of 1 $M_\odot$, 2 $M_\odot$, and 3 $M_\odot$, from top to bottom, are shown for their respective five companion masses in various colors and line styles.

5 Conclusions

5.1 Summary

This work investigates the effect of convection on the theoretical light curves for common envelope events. Convection has been shown to be a necessary ingredient that is often neglected in CE modeling. RGB/AGB stars have deep convective envelopes, capable of transporting the liberated orbital energy to the surface of the star faster then the orbit decays. This in turn allows the CE to radiatively cool and self-regulate. When convection is included, the observed galactic distributions of white dwarf + M dwarfs, double white dwarfs, and Wolf-Rayet binaries are reproduced. In this work, we produced theoretical light curves of convective common envelopes. The time-evolution of the luminosity comes from two distinct phases: the inspiral dynamics, and a plateau phase that occurs once the envelope is ejected. This yields a gradual increase in light that starts once the companion has entered the primary star's envelope. Convection in the star's outer layers carries energy (and therefore luminosity) to the surface. This differs from current modeling techniques that show no gradual increase but an immediate pulse to the plateau phase due to ejection (Figure 17).

These light curves allow for calculations of flux densities at each point in time of these events, which, coupled with a distance, allow for direct comparisons to the Vera C. Rubin observatory telescope bands. This means the models will match directly to data from the observatory. Given CE rates in the galaxy ($\sim$1 per year), it is likely the Rubin observatory will detect a CE event in the future.

5.2 Future Work

Looking ahead, one of the main efforts of this project will be to expand the modeled systems beyond those of the 1 $M_\odot$, 2 $M_\odot$, and 3 $M_\odot$ primary stars, so that, when the Vera C. Rubin observatory's data becomes public, any variations on these shortened time scales can be calculated and matched. Along with comparison to future data, the light curves can be compared to already observed ILOT events, as described in Section 4.4. This means the first observed and confirmed common envelope event may only be several years away from being

discovered.

The light curves are not the end of the project. Currently, efforts to calculate the apparent magnitude of the sources for another means of direct comparison to the results of the instrument are underway. The process is explained below in Section 5.2.1.

Other projects are also listed in Section 5.2.2.

5.2.1 Vera C. Rubin Observatory Models

At this point, for each moment in time of this event, calculations thus far have provided the radius and luminosity of the system. Using the relationship between luminosity, radius and temperature ($L = 4\pi R^2 \sigma T^4$), the surface temperature of these systems at each point in time can also be calculated. With these three values, one can derive the flux using a Blackbody approximation for each moment in time, which can in turn be used to calculate the apparent magnitude of the sources and determine whether they will be visible across the observing bands of the Vera C. Rubin Observatory instrument (Željko Ivezić *et al.* (2008)). This step will allow for direct comparison between observed data and these theoretical light curve models to confirm a CE event.

5.2.2 Beyond Light Curves

Other work related to common envelope event modeling efforts, but not directly to light curves, will include working with AstroBEAR (Cunningham *et al.* (2009)) to aid in modeling efforts on the fluid dynamics of these systems.

An extension of this, with help from Professor Joel Kastner, also includes modeling the three (or possibly four) body system V4046 Sagittarii (Sgr), a close binary system surrounded by a substantially massive disk and a third body (also possibly in its own binary system) orbiting the system much further away (Kastner *et al.* (2011); Rapson *et al.* (2015); Ruíz-Rodríguez *et al.* (2019); Martinez-Brunner *et al.* (2022)). In combining common envelope evolution with a simplified three-body modeling software like REBOUND (IAS15 integrator, Rein & Spiegel (2015)), the goal would be two-fold: to see if the methods of this thesis can

accurately recreate the close binary system of V4046 Sgr, as well as discovering what physical properties allow for a third-body and a massive disk (theory predicts that third bodies usually disrupt disks around binaries and leave their surroundings rather bare, but this is not what has been observed in this system (Kastner *et al.* (2011))).

Bibliography

2007 (6). *Hertzsprung-Russell Diagram.* 1

Abbott, B. P., *et al.* 2016. Binary Black Hole Mergers in the First Advanced LIGO Observing Run. *Physical Review X*, **6**, 041015. 2.1

Abbott, R., *et al.* 2020. GW190521: A Binary Black Hole Merger with a Total Mass of 150 M. *Physical Review Letters*, **125**(9), 101102. 2.1

Abbott, R., *et al.* 2021. Observation of Gravitational Waves from Two Neutron Star–Black Hole Coalescences. *The Astrophysical Journal Letters*, **915**(6), L5. 2.1

Arnett, W.D. 1980. Analytic solutions for light curves of supernovae of Type II. *The Astrophysical Journal*, **237**(4), 541–549. 4.1.1

Bloecker, T. 1995. Stellar evolution of low and intermediate-mass stars. I. Mass loss on the AGB and its consequences for stellar evolution. - NASA/ADS. *Astronomy and Astrophysics*, **297**(5), 727. 3.1

Canals, Pere, Torres, Santiago, & Soker, Noam. 2018. Oxygen-neon-rich merger during common envelope evolution. *Monthly Notices of the Royal Astronomical Society*, **480**(11), 4519–4525. 2.1

Chamandy, Luke, Frank, Adam, Blackman, Eric G., Carroll-Nellenback, Jonathan, Liu, Baowei, Tu, Yisheng, Nordhaus, Jason, Chen, Zhuo, & Peng, Bo. 2018a. Accretion in common envelope evolution. *Monthly Notices of the Royal Astronomical Society*, **480**(10), 1898–1911. 2.2, 2.2.1, 3

Chamandy, Luke, Tu, Yisheng, Blackman, Eric G., Carroll-Nellenback, Jonathan, Frank, Adam, Liu, Baowei, & Nordhaus, Jason. 2018b. Energy Budget and Core-Envelope Motion in Common Envelope Evolution. *Monthly Notices of the Royal Astronomical Society*, **486**(12), 1070–1085. 2.2.1

Chen, Zhuo, Frank, Adam, Blackman, Eric G., Nordhaus, Jason, & Carroll-Nellenback, Jonathan. 2017. Mass transfer and disc formation in agb binary systems. *Monthly Notices of the Royal Astronomical Society*, **468**(7), 4465–4477. 2.1.1

Chugai, N. N. 1991. Duration of the Plateau Stage in Type-II Supernovae - NASA/ADS. *Soviet Astronomy Letters*, **17**(5). 4

Cunningham, Andrew J., Frank, Adam, Varnière, Peggy, Mitran, Sorin, & Jones, Thomas W. 2009. Simulating Magnetohydrodynamical Flow With Constrained Transport and Adaptive Mesh Refinement: Algorithms and Tests of the AstroBEAR Code. *The Astrophysical Journal Supplement Series*, **182**(5), 519. 5.2.2

Davis, P. J., Kolb, U., & Willems, B. 2009. A comprehensive population synthesis study of post-common envelope binaries. *Monthly Notices of the Royal Astronomical Society*, **403**(3), 179–195. 2.2.1

Duchêne, Gaspard, & Kraus, Adam. 2013. Stellar Multiplicity. *http://dx.doi.org/10.1146/annurev-astro-081710-102602*, **51**(8), 269–310. 1.2

Dunham, Michael M., Stutz, Amelia M., Allen, Lori E., Evans, Neal J., Fischer, William J., Megeath, S. Thomas, Myers, Philip C., Offner, Stella S. R., Poteet, Charles A., Tobin, John J., & Vorobyov, Eduard I. 2014 (1). *The Evolution of Protostars: Insights from Ten Years of Infrared Surveys with Spitzer and Herschel*. 1.1.1

Fabrycky, Daniel, & Tremaine, Scott. 2007. Shrinking Binary and Planetary Orbits by Kozai Cycles with Tidal Friction. *The Astrophysical Journal*, **669**(11), 1298–1315. 2.1

Fernie, J D. 1969. The Period-Luminosity Relation: A Historical Review. *Publications of the Astronomical Society of the Pacific*, **81**(12), 707. 1

Galaviz, Pablo, Marco, Orsola De, Passy, Jean-Claude, Staff, Jan E., & Iaconi, Roberto. 2017. Common Envelope Light Curves. I. Grid-code Module Calibration. *The Astrophysical Journal Supplement Series*, **229**(4), 36. 3

Glanz, Hila, & Perets, Hagai B. 2018. Efficient common-envelope ejection through dust-driven winds. *Monthly Notices of the Royal Astronomical Society: Letters*, **478**(7), L12–L17. 2.2.1

Grichener, Aldana, Sabach, Efrat, & Soker, Noam. 2018. The limited role of recombination energy in common envelope removal. *Monthly Notices of the Royal Astronomical Society*, **478**(8), 1818–1824. 2.2, 2.2.1

Hatfull, Roger W.M., Ivanova, Natalia, & Lombardi, James C. 2021. Simulating a stellar contact binary merger - I. Stellar models. *Monthly Notices of the Royal Astronomical Society*, **507**(10), 385–397. 3, 4, 4.2, 17

Herwig, Falk. 2005. Evolution of Asymptotic Giant Branch Stars. *Annual Review of Astronomy Astrophysics*, **43**(9), 435–479. 1.1.4

Hosokawa, Takashi, & Omukai, Kazuyuki. 2009. Evolution of Massive Protostars with High Accretion Rates. *The Astrophysical Journal*, **691**(1), 823. 1.1.1

Hoyle, F., & Lyttleton, R. A. 1939. The evolution of the stars. *Nature*, **144**(12), 1019–1020. 1.1.1

Iaconi, Roberto, & de Marco, Orsola. 2019. Speaking with one voice: Simulations and observations discuss the common envelope parameter. *Monthly Notices of the Royal Astronomical Society*, **490**(12), 2550–2566. 3

Iben, I., & Tutukov, A. V. 1984. The evolution of low-mass close binaries influenced by the radiation of gravitational waves and by a magnetic stellar wind. *The Astrophysical Journal*, **284**(9), 719–744. 2.2

Iben, Jr Icko. 1967. Stellar Evolution Within and Off the Main Sequence. *Annual Review of Astronomy and Astrophysics*, **5**(9), 571–626. 1.1.2

Icko, Jr. Iben, & Livio, Mario. 1993. Common envelopes in binary star evolution. *Publications of the Astronomical Society of the Pacific*, **105**(12), 1373. 2.2

Ivanova, N., Justham, S., Chen, X., Marco, O. De, Fryer, C. L., Gaburov, E., Ge, H., Glebbeek, E., Han, Z., Li, X. D., Lu, G., Marsh, T., Podsiadlowski, Ph., Potter, A., Soker, N., Taam, R., Tauris, T. M., van den Heuvel, E. P. J., & Webbink, R. F. 2012. Common Envelope Evolution: Where we stand and how we can move forward. *The Astronomy and Astrophysics Review*, **21**(9), 1–83. 2.1.1, 6

Ivanova, N., Justham, S., Nandez, J. L. Avendano, & Lombardi, J. C. 2013. Identification of the long-sought common-envelope events. *Science*, **339**(1), 433–435. 3, 4

Ivanova, N., Justham, S., & Podsiadlowski, Ph. 2015. On the role of recombination in common-envelope ejections. *Monthly Notices of the Royal Astronomical Society*, **447**(3), 2181–2197. 2.2, 2.2.1

Ivanova, Natalia. 2018. On the Use of Hydrogen Recombination Energy during Common Envelope Events. *The Astrophysical Journal*, **858**(5), L24. 2.2, 2.2.1

Kasen, Daniel, & Woosley, S. E. 2009. Type II supernovae: Model light curves and standard candle relationships. *The Astrophysical Journal*, **703**, 2205–2216. 4

Kashi, Amit, & Soker, Noam. 2016. An intermediate-luminosity-optical-transient (ILOT) model for the young stellar object ASASSN-15qi. *Monthly Notices of the Royal Astronomical Society*, **468**(9), 4938–4943. 3

Kashi, Amit, & Soker, Noam. 2018. Counteracting tidal circularization with the grazing envelope evolution. *Monthly Notices of the Royal Astronomical Society*, **480**(11), 3195–3200. 2.2.1

Kastner, J H, Sacco, G G, Montez, R, Huenemoerder, D P, Shi, H, Alecian, E, Argiroffi, C, Audard, M, Bouvier, J, Damiani, F, Donati, J.-F, Gregory, S G, Udel, M G ¨, Hussain, G A J, Maggio, A, & Montmerle, T. 2011. A Wide-Separation Companion to the Close T Tauri Binary System V4046 Sgr AB. *The Astrophysical Journal Letters*, **740**, 17. 5.2.2

Kastner, Joel H., & Wilson, Emily. 2021. Detached Shell Carbon Stars: Tracing Thermal Pulses on the Asymptotic Giant Branch. *The Astrophysical Journal*, **922**(11), 24. 1.1.4

Kippenhahn, Rudolf, Weigert, Alfred, & Weiss, Achim. 2012. *Stellar Structure and Evolution.* Second edn. Springer Berlin Heidelberg. 1.1.1, 1.1.4

Kochanek, C. S., Adams, Scott M., & Belczynski, Krzysztof. 2014. Stellar mergers are common. *Monthly Notices of the Royal Astronomical Society*, **443**, 1319–1328. 2.1.1

Kruckow, Matthias U., Tauris, Thomas M., Langer, Norbert, Kramer, Michael, & Izzard, Robert G. 2018. Progenitors of gravitational wave mergers: Binary evolution with the stellar grid-based code COMBINE. *Monthly Notices of the Royal Astronomical Society*, **481**(12), 1908–1949. 2.1

Kuruwita, Rajika L., Staff, Jan, & Marco, Orsola De. 2016. Considerations on the role of fall-back discs in the final stages of the common envelope binary interaction. *Monthly Notices of the Royal Astronomical Society*, **461**(9), 486–496. 2.2.1

Larson, Richard B. 2003. *The physics of star formation.* 1.1.1

Lau, Mike Y.M., Hirai, Ryosuke, González-Bolívar, Miguel, Price, Daniel J., Marco, Orsola De, & Mandel, Ilya. 2022. Common envelopes in massive stars: towards the role of radiation pressure and recombination energy in ejecting red supergiant envelopes. *Monthly Notices of the Royal Astronomical Society*, **512**(4), 5462–5480. 2.2.1

Liebert, James. 1980. White Dwarf Stars. *Annual Review of Astronomy and Astrophysics*, **18**(11), 363–398. 1.1.5

Livio, Mario, & Soker, Noam. 1988. The Common Envelope Phase in the Evolution of Binary Stars. *The Astrophysical Journal*, **329**(6), 764. 2.2

Marco, Orsola De, Passy, Jean Claude, Moe, Maxwell, Herwig, Falk, Low, Mordecai Mark Mac, & Paxton, Bill. 2011. On the formalism for the common envelope interaction. *Monthly Notices of the Royal Astronomical Society*, **411**, 2277–2292. 2.1.1, 2.2, 3.2.1

Martinez-Brunner, Rafael, Casassus, Simon, Pérez, Sebastián, Hales, Antonio, Weber, Philipp, Carcamo, Miguel, Arce-Tord, Carla, Cieza, Lucas, Garufi, Antonio, Marino, Sebastián, & Zurlo, Alice. 2022. High-resolution ALMA observations of V4046 Sgr: a circumbinary disc with a thin ring. *MNRAS*, **510**, 1248–1257. 5.2.2

Mazzali, Paolo A, Röpke, Friedrich K, Benetti, Stefano, & Hillebrandt, Wolfgang. 2007. A Common Explosion Mechanism for Type Ia Supernovae. *Science*, **315**(2), 825–828. 1.1.6

Michaely, Erez, & Perets, Hagai B. 2016. Tidal capture formation of low-mass X-ray binaries from wide binaries in the field. *Monthly Notices of the Royal Astronomical Society*, **458**(3), 4188–4197. 2.1

Nandez, Jose L. A., Ivanova, Natalia, & Lombardi, James C. 2015. Recombination energy in double white dwarf formation. *Monthly Notices of the Royal Astronomical Society*, **450**(3), L39–L43. 2.2, 2.2.1

Nordhaus, J., & Blackman, E. G. 2006. Low-mass binary-induced outflows from asymptotic giant branch stars. *Monthly Notices of the Royal Astronomical Society*, **370**(8), 2004–2012. 2.1.1, 3.2, 3.2.1

Nordhaus, J., & Spiegel, D. S. 2013. On the orbits of low-mass companions to white dwarfs and the fates of the known exoplanets. *Monthly Notices of the Royal Astronomical Society*, **432**(6), 500–505. 3.1

Nordhaus, J., Blackman, E. G., & Frank, A. 2007. Isolated vs. Common Envelope Dynamos in Planetary Nebula Progenitors. *Monthly Notices of the Royal Astronomical Society*, **376**(4), 599–608. 3.2

Nordhaus, J., Spiegel, D. S., Ibgui, L., Goodman, J., & Burrows, A. 2010. Tides and Tidal Engulfment in Post-Main Sequence Binaries: Period Gaps for Planets and Brown Dwarfs Around White Dwarfs. *MNRAS*, **408**(10), 631–641. 2.1.1, 3.1

Nordhaus, Jason, Wellons, Sarah, Spiegel, David S., Metzger, Brian D., & Blackman, Eric G. 2011. Formation of high-field magnetic white dwarfs from common envelopes. *Proceedings*

of the National Academy of Sciences of the United States of America, **108**(2), 3135–3140. 2.1.1

Ohlmann, Sebastian T., Röpke, Friedrich K., Pakmor, Rüdiger, & Springel, Volker. 2015. Hydrodynamic Moving-Mesh Simulations of the Common Envelope Phase in Binary Stellar Systems. *The Astrophysical Journal Letters*, **816**(12), L9. 2.2.1, 3

Paczynski, B. 1976. Structure and Evolution of Close Binary Systems. D. Reidel Publishing Co. 2.1

Palla, Francesco. 2012 (9). 1961-2011: Fifty years of Hayashi tracks. vol. 1480. 1.1.2

Park, KwangHo, & Bogdanović, Tamara. 2017. Gaseous Dynamical Friction in Presence of Black Hole Radiative Feedback. *The Astrophysical Journal*, **838**(3), 103. 3.2

Passy, Jean-Claude, Marco, Orsola De, Fryer, Chris L., Herwig, Falk, Diehl, Steven, Oishi, Jeffrey S., Low, Mordecai-Mark Mac, Bryan, Greg L., & Rockefeller, Gabriel. 2011. Simulating the Common Envelope Phase of a Red Giant Using SPH and Uniform Grid Codes. *The Astrophysical Journal*, **744**(7), 52. 2.2.1, 3

Paxton, Bill, Bildsten, Lars, Dotter, Aaron, Herwig, Falk, Lesaffre, Pierre, & Timmes, Frank. 2011. Modules for Experiments in Stellar Astrophysics (MESA). *Astrophysical Journal, Supplement Series*, **192**(1), 3. 3.1

Paxton, Bill, Schwab, Josiah, Bauer, Evan B., Bildsten, Lars, Blinnikov, Sergei, Duffell, Paul, Farmer, R., Goldberg, Jared A., Marchant, Pablo, Sorokina, Elena, Thoul, Anne, Townsend, Richard H. D., & Timmes, F. X. 2018. Modules for Experiments in Stellar Astrophysics (MESA): Convective Boundaries, Element Diffusion, and Massive Star Explosions. *ApJS*, **234**(10), 34. 3.1

Politano, Michael, & Weiler, Kevin P. 2007. Population Synthesis Studies of Close Binary Systems Using a Variable Common Envelope Efficiency Parameter: I. Dependence upon Secondary Mass. *The Astrophysical Journal*, **665**(2), 663–679. 2.1.1, 2.2.1

Popov, D. V. 1993. An analytical model for the plateau stage of Type II supernovae. *The Astrophysical Journal*, **414**(9), 712. 4, 4.1

Rapson, Valerie A, Sargent, Benjamin, Sacco, G Germano, Kastner, Joel H, Wilner, David, Rosenfeld, Katherine, Andrews, Sean, Herczeg, Gregory, Marel, Nienke Van Der, He, Yi, Lu, Yuan, & Qu, Haidian. 2015. A Combined Spitzer and Herschel Infrared Study of Gas and Dust in the Circumbinary Disk Orbiting V4046 Sgr. *The Astrophysical Journal*, **810**, 14. 5.2.2

Reichardt, Thomas A., Marco, Orsola De, Iaconi, Roberto, Chamandy, Luke, & Price, Daniel J. 2020. The impact of recombination energy on simulations of the common-envelope binary interaction. *Monthly Notices of the Royal Astronomical Society*, **494**(6), 5333–5349. 2.2.1

Reimers, D. 1975. Circumstellar absorption lines and mass loss from red giants. - NASA/ADS. *Memoires of the Societe Royale des Sciences de Liege*, **8**, 369–382. 3.1

Rein, Hanno, & Spiegel, David S. 2015. IAS15: A fast, adaptive, high-order integrator for gravitational dynamics, accurate to machine precision over a billion orbits. *MNRAS*, **446**, 1424–1437. 5.2.2

Ricker, Paul M., & Taam, Ronald E. 2008. The Interaction of Stellar Objects within a Common Envelope. *The Astrophysical Journal*, **672**(1), L41–L44. 2.2.1

Ricker, Paul M., & Taam, Ronald E. 2012. An AMR study of the common-envelope phase of binary evolution. *The Astrophysical Journal*, **746**(2), 74. 2.2.1, 3

Ruíz-Rodríguez, Dary, Kastner, Joel H, Dong, Ruobing, Principe, David A, Andrews, Sean M, & Wilner, David J. 2019. Constraints on a Putative Planet Sculpting the V4046 Sagittarii Circumbinary Disk. *The Astronomical Journal*, **157**(6), 237. 5.2.2

Sabach, Efrat, Hillel, Shlomi, Schreier, Ron, & Soker, Noam. 2017. Energy transport by convection in the common envelope evolution. *Monthly Notices of the Royal Astronomical Society*, **472**, 4361–4367. 2.2.1

Schreier, Ron, Hillel, Shlomi, Shiber, Sagiv, & Soker, Noam. 2021. Simulating highly eccentric common envelope jet supernova impostors. *Monthly Notices of the Royal Astronomical Society*, **508**(10), 2386–2398. 2.2.1

Shappee, Benjamin J., & Thompson, Todd A. 2013. The mass-loss-induced eccentric Kozai mechanism: A new channel for the production of close compact object-stellar binaries. *The Astrophysical Journal*, **766**(3), 64. 2.1

Soker, Noam. 2015. Close Stellar Binary Systems by Grazing Envelope Evolution. *The Astrophysical Journal*, **800**(2), 114. 2.2.1

Soker, Noam, & Kashi, Amit. 2011. Formation of Bipolar Planetary Nebulae by Intermediate-Luminosity Optical Transients. *The Astrophysical Journal*, **746**(8), 100. 4.4

Soker, Noam, Grichener, Aldana, & Sabach, Efrat. 2018. Radiating the Hydrogen Recombination Energy during Common Envelope Evolution. *The Astrophysical Journal*, **863**(8), L14. 2.2, 2.2.1

Thompson, Todd A. 2011. Accelerating compact object mergers in triple systems with the Kozai resonance: A mechanism for "prompt" type Ia supernovae, gamma-ray bursts, and other exotica. *The Astrophysical Journal*, **741**(11), 82. 2.1

Toonen, S., Hollands, M., Gänsicke, B. T., & Boekholt, T. 2017. The binarity of the local white dwarf population. *Astronomy and Astrophysics*, **602**(6), A16. 2.2.1

Toonen, Silvia, & Nelemans, Gijs. 2013. The effect of common-envelope evolution on the visible population of post-common-envelope binaries. *Astronomy Astrophysics*, **557**(9), A87. 2.1

Tutukov, A, & Yungelson, L. 1979. Evolution of massive common envelope binaries and mass loss. - NASA/ADS. D. Reidel Publishing Co. 2.2

Villaver, Eva, & Livio, Mario. 2009. The orbital evolution of gas giant planets around giant stars. *The Astrophysical Journal*, **705**(11), L81–L85. 3.1

Webbink, R. F. 1984. Double white dwarfs as progenitors of R Coronae Borealis stars and type I supernovae. *The Astrophysical Journal*, **277**(2), 355–360. 2.2

Weiler, Kurt W., & Sramek, Richard A. 1988. Supernovae and Supernova Remnants. *Annual Review of Astronomy and Astophysics*, **26**(11), 295–341. 1.1.6

Wilson, E. C., & Nordhaus, J. 2019. The role of convection in determining the ejection efficiency of common envelope interactions. *Monthly Notices of the Royal Astronomical Society*, **485**(3), 4492–4501. 2.2, 2.2.1, 2.2.2, 2.2.2, 8, 3, 3.2, 3.2.1

Wilson, E. C., & Nordhaus, J. 2020. Convection and spin-up during common envelope evolution: The formation of short-period double white dwarfs. *Monthly Notices of the Royal Astronomical Society*, **497**(9), 1895–1903. 2.2, 2.2.1, 2.2.2, 3

Wilson, E. C., & Nordhaus, J. 2022. Convection Reconciles the Difference in Efficiencies Between Low-Mass and High-Mass Common Envelopes. *Monthly Notices of the Royal Astronomical Society*, 3. 2.2.1, 2.2.2, 3

Yan, Hong-Liang, Zhou, Yu-Tao, Zhang, Xianfei, Yaguang, Gao, Qi, Shi, Jian-Rong, Zhao, Gang, Aoki, Wako, Matsuno, Tadafumi, Li, Yan, Xu, Xiao-Dong, Li, Haining, Wu, Ya-Qian, Jin, Meng-Qi, Mosser, Benoit, Bi, Shao-Lan, Fu, Jian-Ning, Pan, Kaike, Suda, Takuma, Liu, Yu-Juan, Zhoa, Jing-Kun, & Lian, Xi-Long. 2020 (10). *Evolutionary Status of Extremely Li-Enhanced Red Giants | Obsevation Results | Subaru Telescope*. 4

Yarza, Ricardo, Lopez, Naela Razo, Murguia-Berthier, Ariadna, Everson, Rosa Wallace, Antoni, Andrea, MacLeod, Morgan, Soares-Furtado, Melinda, Lee, Dongwook, & Ramirez-Ruiz, Enrico. 2022. Hydrodynamics and survivability during post-main-sequence planetary engulfment. *arXiv*, 3. 3.2.1

Zorotovic, M., Schreiber, M. R., Gänsicke, B. T., & Gómez-Morán, A. Nebot. 2010. Post-common-envelope binaries from SDSS. IX: Constraining the common-envelope efficiency. *Astronomy and Astrophysics*, **520**(6), A86. 2.2.1

Zorotovic, M., Schreiber, M. R., Gänsicke, B. T., Rebassa-Mansergas, A., Gómez-Morán, A. Nebot, Southworth, J., Schwope, A. D., Pyrzas, S., Rodríguez-Gil, P., Schmidtobreick, L., Schwarz, R., Tappert, C., Toloza, O., & Vogt, N. 2011. Post-common-envelope binaries from SDSS. XIII: Mass dependencies of the orbital period distribution. *Astronomy Astrophysics*, **536**(11), L3. 2.1.1

Željko Ivezić, *et al.* 2008. LSST: from Science Drivers to Reference Design and Anticipated Data Products. *The Astrophysical Journal*, **873**(5), 111. 3.1, 5.2.1